Pacific Northwest
NATIONAL LABORATORY

PNNL-29849

Standoff Detection of Chemical Plumes Using Swept-ECQCL Remote Detection Technology

Results from EMRTC Complex Terrain Dual Tracer Experiment

March 2020

Mark C. Phillips
Opticslah, LLC and University of Arizona

Bruce E. Bernacki
Pacific Northwest National Laboratory

Jeremy Yeak
Opticslah, LLC

U.S. DEPARTMENT OF ENERGY

Prepared for the U.S. Department of Energy
under Contract DE-AC05-76RL01830

DISCLAIMER

PACIFIC NORTHWEST NATIONAL LABORATORY
operated by
BATTELLE
for the
UNITED STATES DEPARTMENT OF ENERGY
under Contract DE-AC05-76RL01830

Printed in the United States of America

Available to DOE and DOE contractors from the Office of Scientific and Technical Information,
P.O. Box 62, Oak Ridge, TN 37831-0062
www.osti.gov
ph: (865) 576-8401
fax: (865) 576-5728
email: reports@osti.gov

Available to the public from the National Technical Information Service
5301 Shawnee Rd., Alexandria, VA 22312
ph: (800) 553-NTIS (6847)
or (703) 605-6000
email: info@ntis.gov
Online ordering: http://www.ntis.gov

PNNL-29849

Standoff Detection of Chemical Plumes Using Swept-ECQCL Remote Detection Technology

Results from EMRTC Complex Terrain Dual Tracer Experiment

March 2020

Mark C. Phillips
Opticslah, LLC and University of Arizona

Bruce E. Bernacki
Pacific Northwest National Laboratory

Jeremy Yeak
Opticslah, LLC

Prepared for
the U.S. Department of Energy
under Contract DE-AC05-76RL01830

Pacific Northwest National Laboratory
Richland, Washington 99354

Content

1.0 Introduction

As part of the Complex Terrain Dual Tracer Experiments performed in support of the LYNM program, a swept-wavelength external cavity quantum cascade laser (swept-ECQCL) remote detection system was deployed to measure chemical plume propagation with high temporal resolution. The swept-ECQCL remote detection technology was initially developed at PNNL, and is now under further development at Opticslah, LLC under SBIR funding from DOE (DOE SBIR Phase I Project DE-SC0019855, Remote Detection Technologies, Program Manager Chris Ramos).

The swept-ECQCL technology provides a single-frequency infrared laser source which is rapidly scanned over a large wavelength range to measure the infrared absorption of gases, liquids, or solids. Analysis of the measured infrared absorption spectrum is used to detect, identify, and quantify the chemical species which are present. While most previous laser-based techniques used small wavelength tuning ranges to measure only a few isolated spectral lines of a few species, the swept-ECQCL provides the large tuning range needed to measure multiple species simultaneously, and to detect broad absorption features from large molecules or condensed-phase materials. In addition, the swept-ECQCL systems have high enough spectral resolution and sensitivity to measure narrow lines of small molecules and determine isotope ratios. The remote detection system for gas plumes is based on the swept-ECQCL technology, and consists of a swept-ECQCL source, infrared detector, control electronics, and beam transmitting and alignment optics.

The remote detection system directs the infrared output of the swept-ECQCL to a target retro-reflector typically located at ~10-10,000 m distance. The swept-ECQCL wavelength is varied continuously over a large wavelength range (>1000 nm) at rates up to 1000 Hz. The swept-ECQCL light reflected from the remote target is collected and focused onto an infrared photodetector. By measuring the detector signal continuously as the swept-ECQCL wavelength is varied, a time-series of absorption spectra are measured for the gases along the beam line-of-sight. Based on analysis and fitting of the measured absorption spectra, the time-dependent chemical concentrations of species are determined. Multiple species and mixtures can be detected simultaneously, for all species with absorption features above the sensor noise floor. The sensor output is thus a continuous, high-speed record of identified chemicals along with their concentrations and isotope ratios of interest. The high-speed operation enables low-noise operation in conditions of atmospheric turbulence and allows tracking of fluctuating concentrations in transient chemical plumes as needed for reliable remote detection applications. All components operate with minimal cooling requirements and no cryogens are needed. In addition, the output infrared light is invisible with an intensity below the maximum permissible exposure (MPE) threshold of 100 mW/cm2 for these infrared wavelengths and thus eye safe.

The measurement concept for plume detection using the swept-ECQCL remote detection system is as follows. The ECQCL beam is directed toward a remote retro-reflector, which reflects the beam back to the ECQCL system where it is focused onto an infrared photodetector. The line-of-sight from the ECQCL system to the retro-reflector defines the measurement path. The detected infrared signal is recorded continuously and detects the absorption of molecular species along the measurement path. Before a plume release, the system measures absorption from atmospheric constituents, which in this LWIR band consist primarily of lines from H_2O and CO_2, with additional weaker absorption from N_2O, NH_3, and O_3 possibly contributing. The system then measures any changes in absorption due to the tracer

compounds when they enter the measurement path. The shape of absorption features is used to distinguish and identify the different tracer compounds, and the strength of the absorption is used to determine the path-integrated concentration – also called the *column density*.

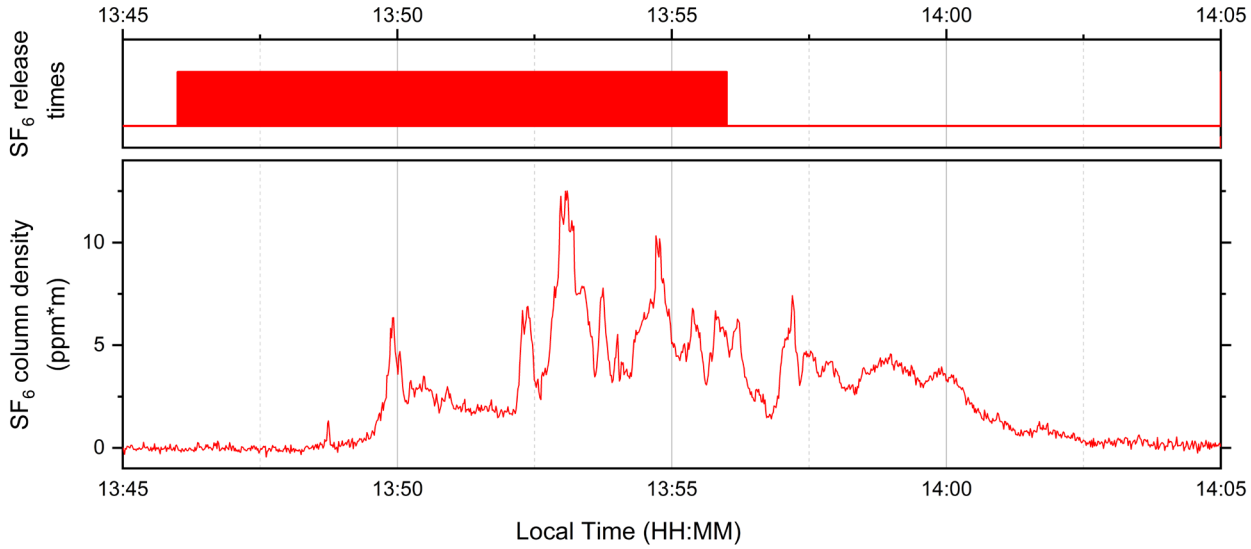

Figure 1: Example measurement data provided by swept-ECQCL remote detection system.

Because the measurement is "path-integrated" it cannot determine where along the measurement path the tracer compounds are located only that they are present somewhere along the path. Instead, the system provides a continuous and high-speed time-record of column densities for multiple species. Figure 1 shows an example of measurement data acquired by the system. The top panel shows the times at which SF6 was released and the bottom panel shows the column density of SF6 detected along the measurement path. For plume propagation measurements and modeling, the time-resolved column density can provide various types of information such as:

1. ***Time of arrival of the plume at the measurement path.*** The arrival time of the signal at the measurement path can be correlated with the plume release time/duration, distance between release and measurement path, and the local wind conditions.

2. ***Duration of plume intersection with the measurement path.*** The time over which the plume is detected gives information on both the release duration and any temporal "spread" in the plume as it propagates. It may also indicate when the plume propagation is modified by local topographic features.

3. ***Temporal properties of detected column density.*** The detected column density is not typically a uniform rise/fall, but instead shows variations on second- to sub-second time scales. These variations may provide information about local wind conditions and topographic features.

4. ***Magnitude of detected column density.*** The quantitative measurement of time-resolved column density can be compared with plume propagation models. A plume model providing time- and space-resolved plume concentrations can be integrated along the measurement path for direct and quantitative comparison with the measured column density.

5. ***Correlations between different tracers.*** The measurement distinguishes the tracers and can detect them simultaneously even if they are both present. Correlations between the

measured column density for the different tracers can provide information if the release points/times are different or the same.

6. ***Lack of plume detection.*** Given the high sensitivity of detection, if the plume enters the measurement path it will be detected with high confidence. Conversely, if no plume is detected along the measurement path, this negative result indicates that the plume propagated in a direction away from the measurement path. These results can also be correlated with wind data and plume models.

2.0 Measurement Setup and Location

For the experiments performed at EMRTC, a remote detection system initially assembled at PNNL was used. Dr. Phillips is currently using the system at University of Arizona in support of multiple DNN R&D projects, funded via subcontract to PNNL. System modifications were performed by Opticslah under the DOE SBIR project to improve performance for longer-range standoff measurements. The system was transported from Tucson, AZ to EMRTC by automobile in standard Pelican-style shipping cases, and then set up on-site for measurements.

Details of the swept-ECQCL system and operation are provided in Sections 3.0 and 4.0. Four days of testing were performed using the swept-ECQCL remote detection system. From 11/04/2019-11/06/2019, the system was located at the “Little Eagle” site. Figure 2 shows a photograph of the system operating at the Little Eagle site. The Little Eagle site provided a suitable location for the swept-ECQCL system with line power available and a covered area to reduce exposure to the elements. The swept-ECQCL system was co-located with a Telops infrared hyperspectral imaging system, shown in Figure 3.

Figure 2: Photograph of swept-ECQCL remote detection system located at EMRTC “Little Eagle” site.

Figure 3: (left) Photograph of swept-ECQCL system and Telops hyperspectral imaging instrument at Little Eagle site. (Right) Dr. Bruce Bernacki (PNNL) operated the Telops system.

A gold-coated hollow corner cube retro-reflector with 127 mm clear aperture was mounted on a tripod and was placed 1.5 km away from the swept-ECQCL system. Table 1 gives the GPS coordinates of the swept-ECQCL system and the retro-reflector. The calculated distance between the ECQCL and retro-reflector was 1.500 km, with a heading of 129.9582° (relative to N) and an angle of -4.7091° (relative to horizontal). The total measurement path length considering both the forward and return distances was therefore 3000 m. Figure 4 shows photographs of the retroreflector position and the tripod assembly. Placement of the retro-reflector was challenging in the test environment, limited by the site topography and access restrictions. The location required vehicle access and a clear line-of-sight to Little Eagle.

Figure 4: (a) Photograph of valley from swept-ECQCL located at Little Eagle site. The inset shows an image obtained using the visible alignment camera coaligned with the ECQCL beam. The approximate location of the retro-reflector is circled. (b) Photograph of retro-reflector mounted on tripod.

Table 1: GPS coordinates of ECQCL system and retro-reflector for 11/04-11/06.

	ECQCL	Retro-reflector
Latitude (deg) N	34.055219	34.046536
Longitude (deg) W	106.959011	106.946628
Elevation (m)	1758	1635

Figure 5 shows an overhead view and Figure 6 shows a side view of the measurement configuration, obtained from Google Earth. The ECQCL system and retro-reflector positions are marked, as are various plume release points. The tracers on 11/04 and 11/05 were released from sites CB (cliff bottom) and CT (cliff top). On 11/06, tracers were released primarily from sites VG (valley gate) and ERB (entry-road bend). All the release points were located toward the retro-reflector side of the ECQCL measurement path, and the CB and CT locations were very close to the retro-reflector. Figure 7 shows Google Earth images of the measurement path near the retroreflector.

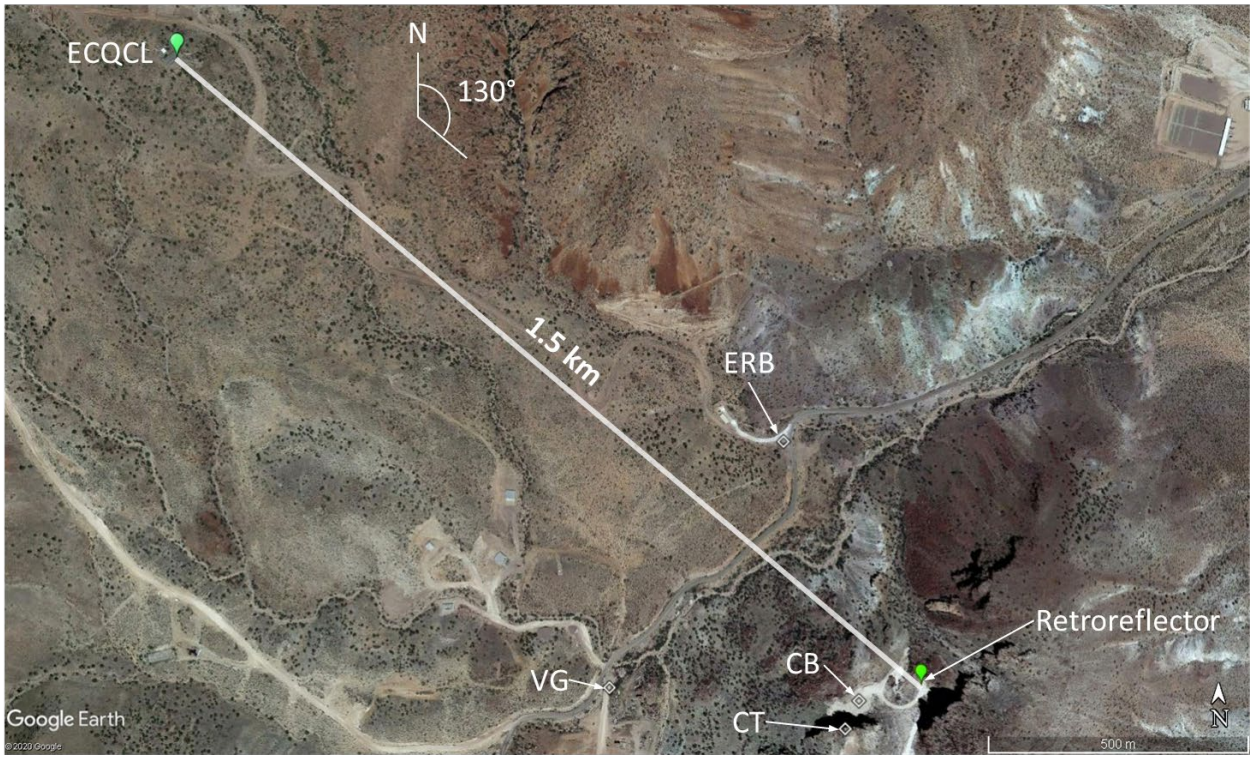

Figure 5: Overhead view for locations of swept-ECQCL, retroreflector, and plume release points for 11/04/2019-11/06/2019.

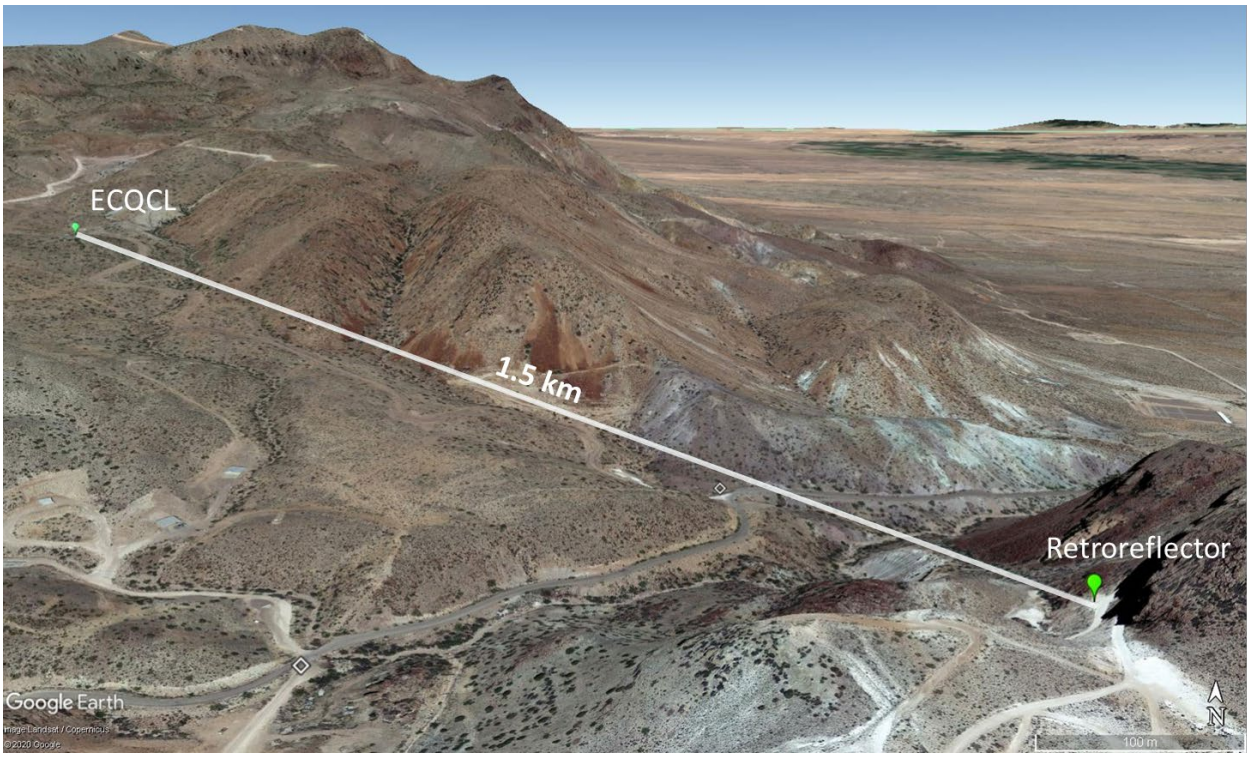

Figure 6: Side view of locations for swept-ECQCL and retroreflector for 11/04/2019-11/06/2019.

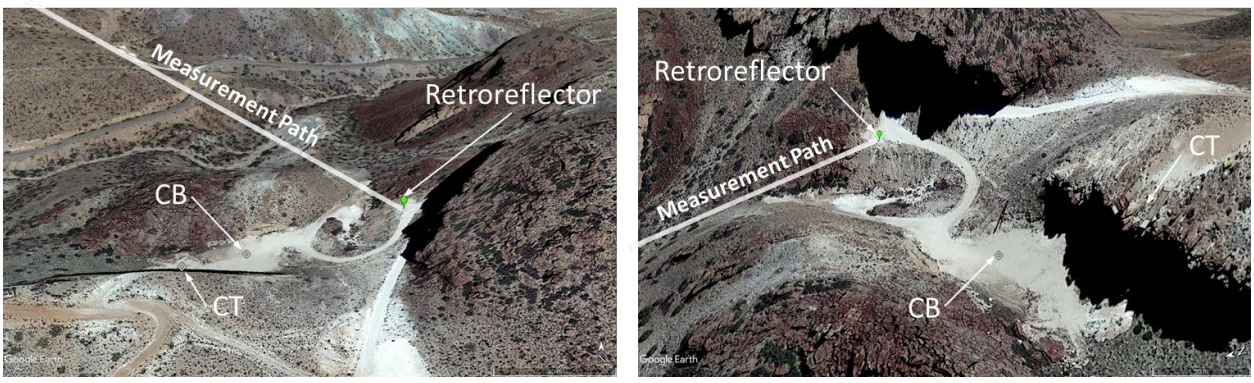

Figure 7: Cliff site details for measurements on 11/04/2019-11/06/2019.

On 11/07, the swept-ECQCL and retro-reflector were moved to a different location called the “Small-arms range”. The calculated distance between ECQCL and the retro-reflector was 188 m, with a heading of 204.2085° relative to N. Figure 8 and Figure 9 show Google Earth images with the ECQCL and retro-reflector locations marked, and Figure 10 shows a photograph of the system set up at the small-arms range.

Error! Reference source not found. shows the GPS coordinates for the ECQCL system and retro-reflector on 11/07. Due to access limitations, the retro-reflector position was not optimal. In particular, the path length was shorter than desired, and the measurement path passed

directly over a roadway. Vehicles driving along the road would therefore block the ECQCL beam, preventing signal from being acquired during these times. Fortunately, the road was not used continuously, resulting on only occasional blocking of the beam.

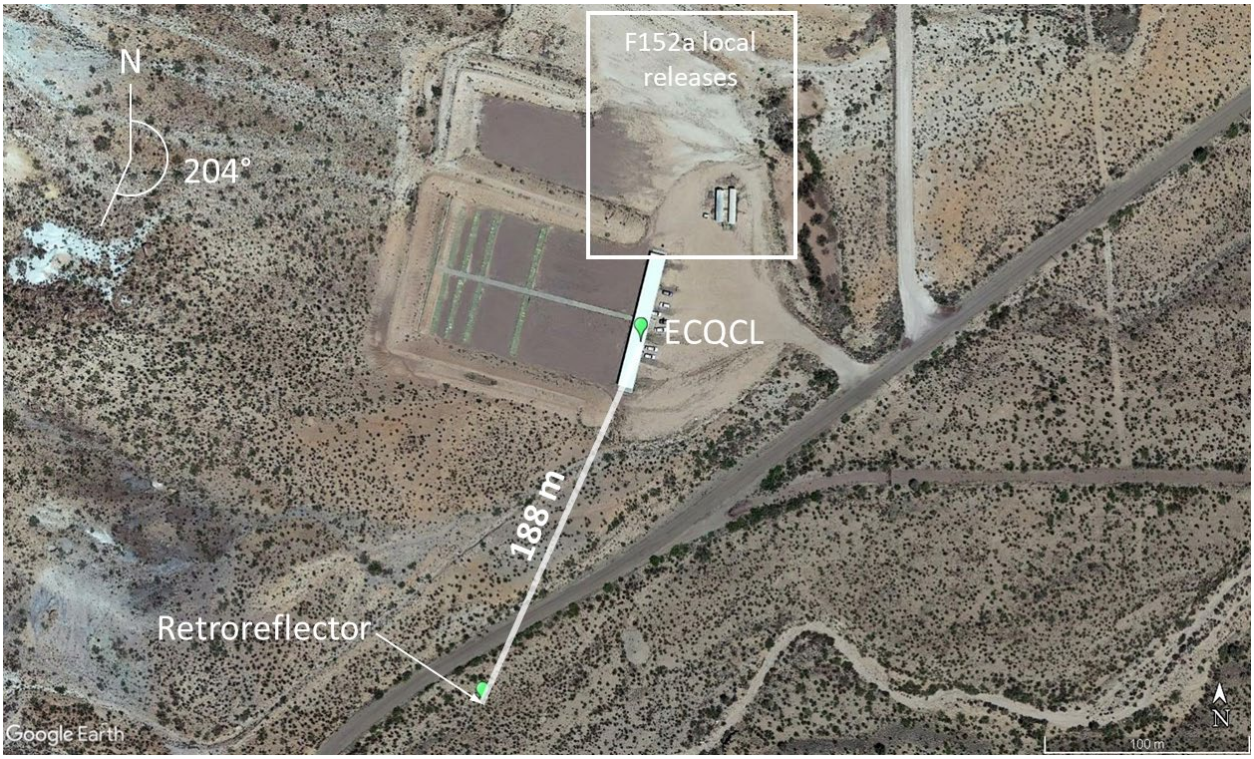

Figure 8: Overhead view for locations of swept-ECQCL, retroreflector, and local testing release points for 11/07/2019.

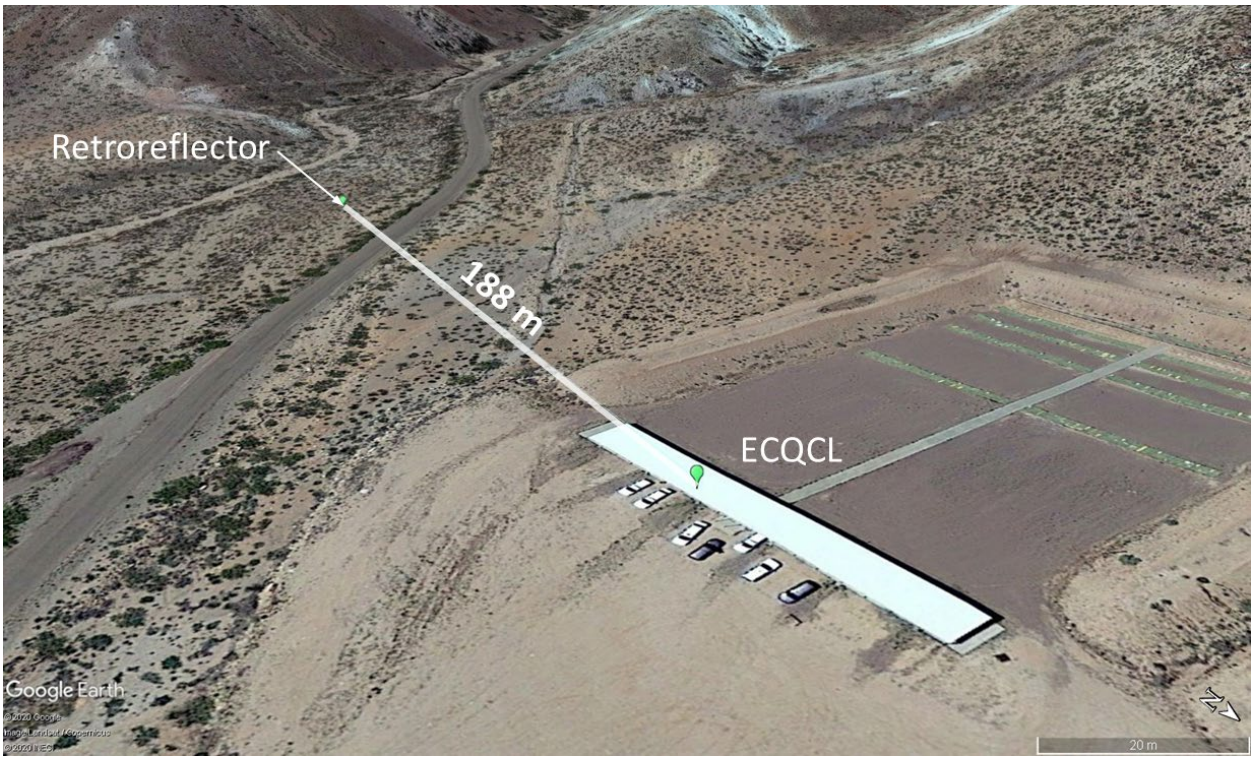

Figure 9: Side view for locations of swept-ECQCL, retroreflector, and local testing release points for 11/07/2019.

Figure 10: Photograph of swept-ECQCL system on 11/07/2019 at “Small-arms range” location.

Table 2: GPS coordinates of ECQCL system and retro-reflector for 11/07.

	ECQCL	Retro-reflector
Latitude (deg) N	34.054603	34.05305
Longitude (deg) W	106.940567	106.941383
Elevation (m)	1505	1508

3.0 System Description

A previous version of the swept-ECQCL standoff detection system was recently described in [1], but a number of system modifications were performed before the testing at EMRTC, which are described in Section 8. Figure 11(a) and Figure 11(b) show schematics of the optical layout for the standoff detection system, and Figure 11(c) shows a photograph. The output from the swept-ECQCL was a collimated beam with diameter ~3 mm ($1/e^2$). A fraction of the beam was reflected from an uncoated BaF_2 wedged window (WW) and directed to an infrared photodetector DET1 (VIGO PVI-4TE-10.6) for a reference measurement of the ECQCL power before propagation over the long atmospheric path. The beam transmitted through the WW was directed to a beam expander consisting of a negative lens L1 and a gold-coated 90° off-axis parabolic (OAP) mirror with 75 mm diameter and f=+230 mm (Thorlabs MPD399-M01). On 11/04 a lens L1 with -25 mm focal length was used; on 11/05-11/07 the L1 was replaced with a lens having -15 mm focal length (no significant differences in performance were observed). The diameter of the expanded launch beam was ~30 mm at the output of the OAP when using L1 with f=-25 mm and the diameter was ~50 mm when using L1 with f=-15 mm. The divergence of the launch beam was adjusted via translation of L1. The launch beam angle was adjusted using a 102 mm diameter protected silver mirror (Steering Mirror) in a gimbal mount located vertically above the launch OAP, as diagrammed in Figure 11(b). Return light from the remote target was aligned onto DET2 (VIGO PVI-4TE-10.6) using a second Steering Mirror and OAP, identical to the launch pair.

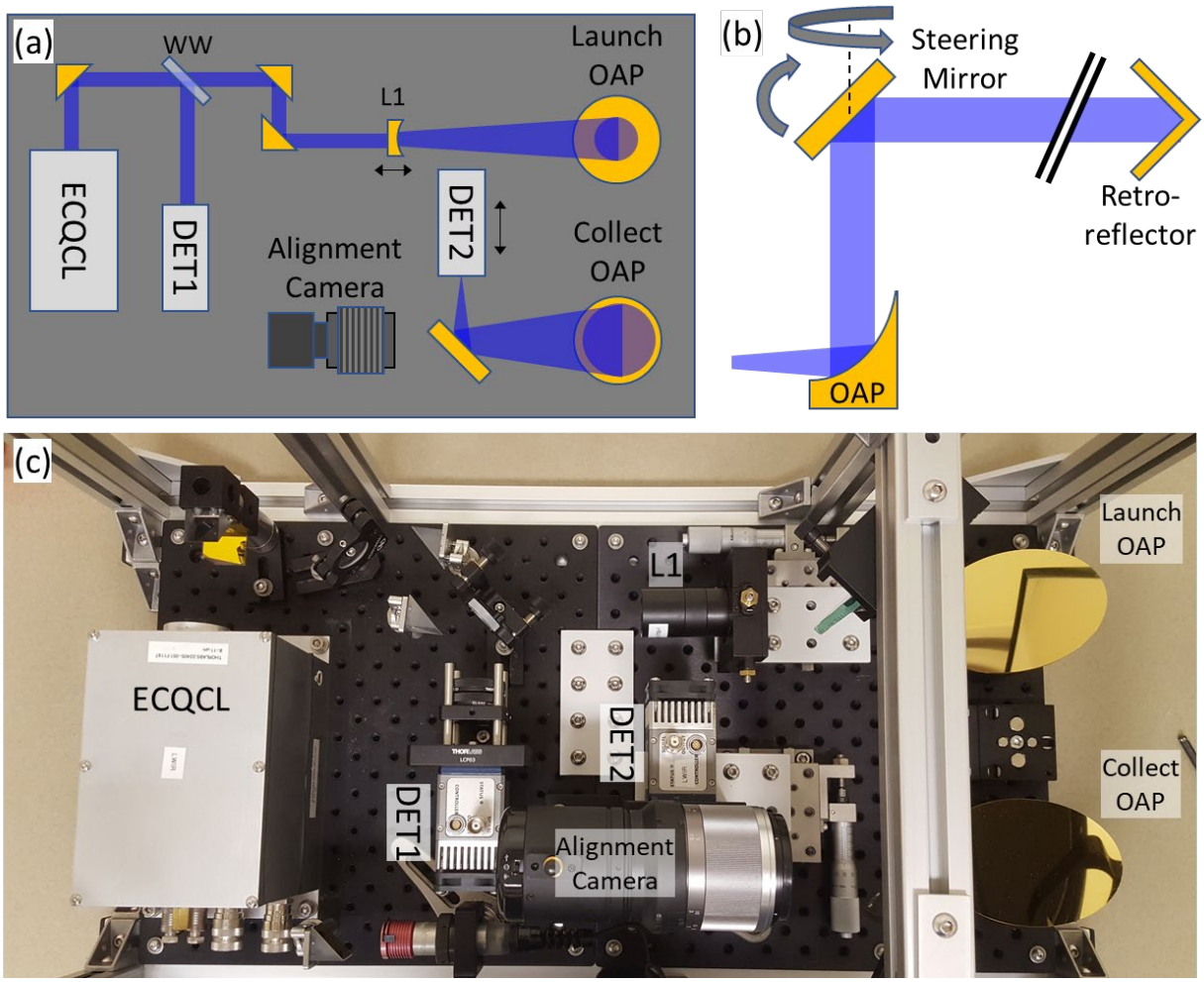

Figure 11: (a) Schematic of standoff detection optical system. (b) Vertical configuration of beam steering optics for alignment of ECQCL beam to a remote retro-reflector target and focusing of return light onto DET2. (c) Photograph of optical system. Additional mirrors on indexed magnetic mounts (not shown) were inserted for coarse alignment using the visible alignment camera and removed for measurements with the ECQCL. Abbreviations: WW – BaF_2 wedged window, L1- Lens, OAP – off-axis parabola, DET1/2 – infrared photodetectors.

Coarse optical alignment of the system was performed by inserting mirrors into the ECQCL beam path to use a visible CMOS alignment camera with 45x telescopic lens (Optex Redtail). The camera was aligned to be co-axial with the ECQCL beam using a close-range target and could be switched into or out of either beam path using indexed mechanical mounts. The alignment camera was placed in each beam path (launch and collection), and the steering mirror angles were aligned to center the retro-reflector image in the camera field of view. After adjustment of the steering mirrors in both launch and collection arms, the alignment camera mirror was removed, allowing the ECQCL beam to propagate to/from the target. This initial course alignment procedure produced a signal on DET2 from a portion of the ECQCL light returned from the retro-reflector. Final optimization of the signal was performed by maximizing the signal on DET2 via iteratively adjusting the launch and collection steering mirrors and adjusting the beam divergence via translation of L1.

4.0 System Operation

Details on operation of the custom-built swept-ECQCL were described in [1], but a brief summary is provided here for completeness. The ECQCL used a QCL device (Thorlabs QE) designed for broadband operation in the LWIR and which provided an overall tuning range of 910-1215 cm^{-1} (8.23-10.99 μm). For the standoff measurements reported here the tuning range was reduced to 915-1200 cm^{-1} (8.33-10.93 μm). The QCL was operated with amplitude-modulation (AM) of the current from 0-1500 mA using a 500 kHz square wave with 50% duty cycle. The output of the ECQCL had a corresponding full-depth AM in intensity at 500 kHz, enabling lock-in detection of the ECQCL signal in the presence of ambient infrared light on the photodetector. The signals on DET1 and DET2 were digitized at a 2 MHz rate using National Instruments hardware and demodulated in software written in LabVIEW, providing measurements of the detected ECQCL intensity at 2 μs intervals.

The swept-ECQCL wavenumber was scanned at a 400 Hz rate (2.5 ms/scan). Although this rate was faster than necessary for tracking the temporal variations in plume concentrations, the fast acquisition rate is beneficial for mitigating effects of atmospheric turbulence. Relative wavenumber calibration was performed by measuring fringes from a solid Si etalon with 0.416 mm thickness (free-spectral range 3.5 cm^{-1}) placed in front of DET1. Calibration of the absolute wavenumber position was performed by comparing a measured absorption spectrum of the atmosphere with a spectrum simulated using HITRAN [2]. After calibration, the 400 Hz scan data included a spectral range of 915-1200 cm^{-1} with 0.1 cm^{-1} spacing. Based on the 2.5 ms needed to scan over the 285 cm^{-1} tuning range, the average tuning rate was 114,000 cm^{-1}/s. The average power of the ECQCL over the 400 Hz scan was 3.5 mW and at the peak of the tuning curve (1125 cm^{-1}) the average power was 6.5 mW. At all times, the intensity was below the maximum permissible exposure (MPE) threshold of 100 mW/cm^2 for these infrared wavelengths.

The scan intensity was converted to absorbance by $A_j(\nu) = -\ln[I_j(\nu)/I_0(\nu)]$ where $I_0(\nu)$ is the average scan intensity for a background data set. Thus, $A_j(\nu)$ measures changes in absorbance relative to the average conditions at the time the background was acquired. A background data set was acquired near the beginning of each day and used for the calculation of absorbance for all data acquired that day. Table 3 lists the data files and times used for the backgrounds. The background region was also used to perform a principal component analysis (PCA) for use in fitting the absorbance spectral baseline, as described in [1]. 20 PC vectors were used for the baseline fitting.

Table 3: Reference data for spectral backgrounds

Date	Background file	Pts	Background start	Background end
110419	110419_135113	0-6000	2:51:24.7818 PM	3:01:24.7899 PM
110519	110519_101324	0-5000	10:13:36.3835 AM	10:21:56.3919 AM
110619	110619_095104	0-3000	9:51:19.7559 AM	9:56:19.7597 AM
110719	110719_102835	1000-7000	10:30:18.5380 AM	10:40:18.5462 AM

Absorbance spectra were analyzed using a weighted least squares (WLS) algorithm, as has been described previously [1]. Library absorption spectra for SF_6 and F152a were obtained from the PNNL/NWIR spectral database [3]. An additional perfluorocarbon tracer species PTCH was added to the analysis library for comparison with prior work [4]. Library absorption spectra

for N_2O, NH_3, H_2O, and CO_2 were modeled using parameters from HITRAN [2]. The HITRAN spectra were convolved with a Gaussian function with 0.3 cm^{-1} full width at half maximum (FWHM) to represent an effective instrument function for the ECQCL scan. The WLS fits were weighted by $I_j(\nu)^2$ to account for increased noise in regions of the spectrum with low detected intensity. The WLS algorithm provides measured column density in units of ppm*m for each species as a function of time. To reduce total computation time for the WLS analysis and to better match the time scales of the plume detections, absorbance spectra were first averaged from the 400 Hz acquisition rate to a 10 Hz rate (40x). For plotting and data delivery, the column densities were further averaged by 10x to a 1 Hz rate.

Figure 12 shows an example of the scan intensity versus wavenumber, $I_0(\nu)$. The overall shape of the profile results from the gain bandwidth of the QCL device used, combined with wavelength-dependent reflectivity of optical elements inside the ECQCL cavity, and finally modified by the wavelength-dependent detector responsivity. The sharp spikes result from absorption by atmospheric H_2O and CO_2 along the 3000 m measurement path. The lower panel of Figure 12 shows simulated absorption spectra for H_2O and CO_2, from the which the various spectral lines in $I_0(\nu)$ may be identified.

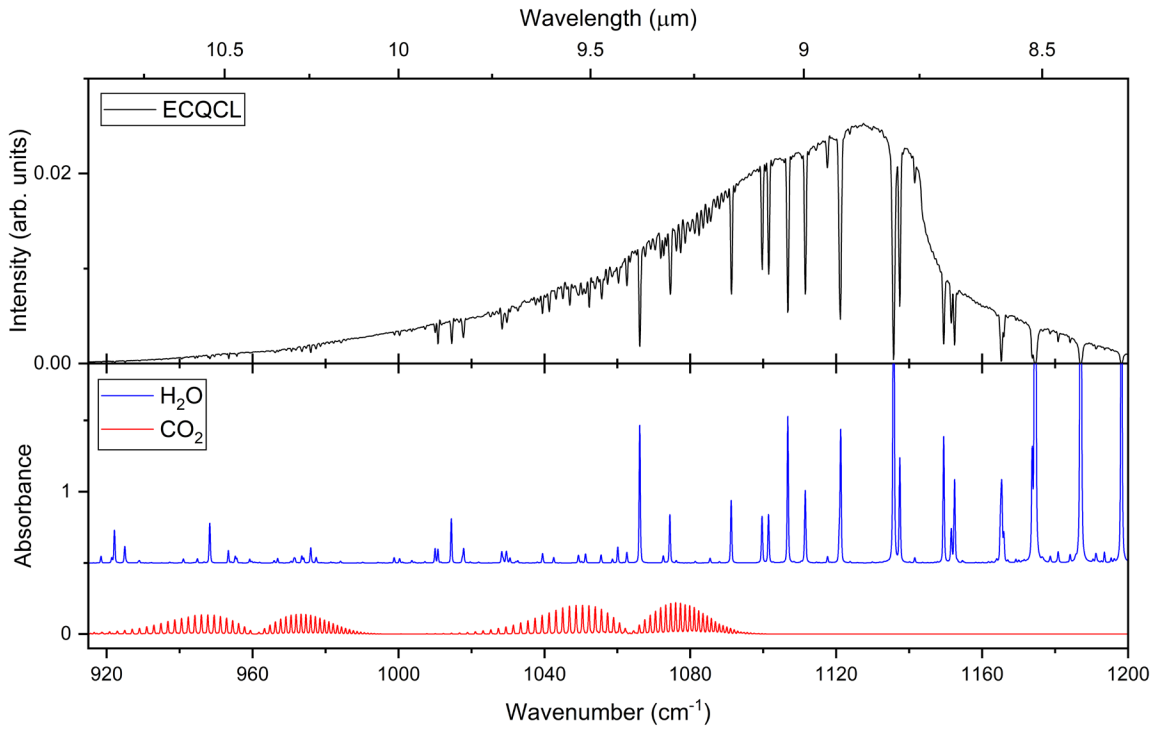

Figure 12: Scan intensity versus wavenumber/wavelength (top) and library spectra for H_2O and CO_2 (bottom).

Figure 13 shows library absorption spectra for the three target gases, plotted over the wavenumber tuning range of the ECQCL. The absorbance is unitless and scaled for a gas concentration of 1 ppm over a pathlength of 1 m. SF_6 has the highest peak absorbance, and thus should be the easiest to detect. F152a has a peak absorbance ~10× less than SF_6 but is still relatively large compared to other gas-phase absorbers. N_2O has a much weaker absorption strength in this wavenumber region, with a peak value ~100× smaller than F152a

and thus is much more difficult to detect. Detection of N_2O would preferably be performed near 2200 cm^{-1} (4.55 μm), where the absorbance is (0.01 ppm*m)$^{-1}$.

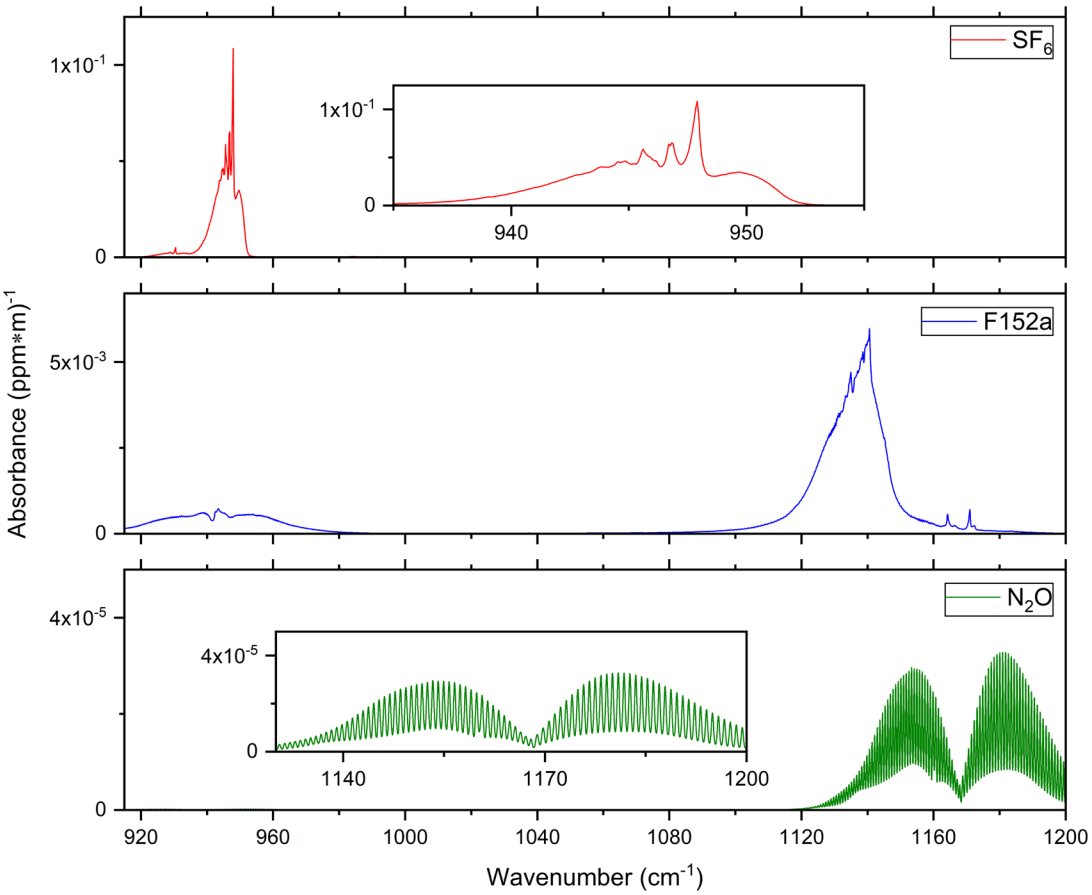

Figure 13: Library absorption spectra for the three target gases over the ECQCL wavenumber scan range. The y-axis shows the absorbance for a 1 ppm concentration over a 1 m path length.

Figure 14 shows examples of absorbance spectra $A_j(\nu) = -\ln[I_j(\nu)/I_0(\nu)]$ in the lower panel, for conditions with no plumes present. The scan intensity $I_0(\nu)$ is shown for reference in the top panel. A series of 4 absorbance spectra are shown, taken from data averaged to 10 Hz. The absorbance spectra exhibit higher noise near the edges of the scan window due to lower power reaching the detector. Unfortunately, the absorption peak for SF_6 is near the edge of the scan window and so falls within a region of higher absorbance noise which in turn increases detection noise. The F152a absorption is closer to the center of the scan window where the power is highest, and the corresponding absorbance noise is lower.

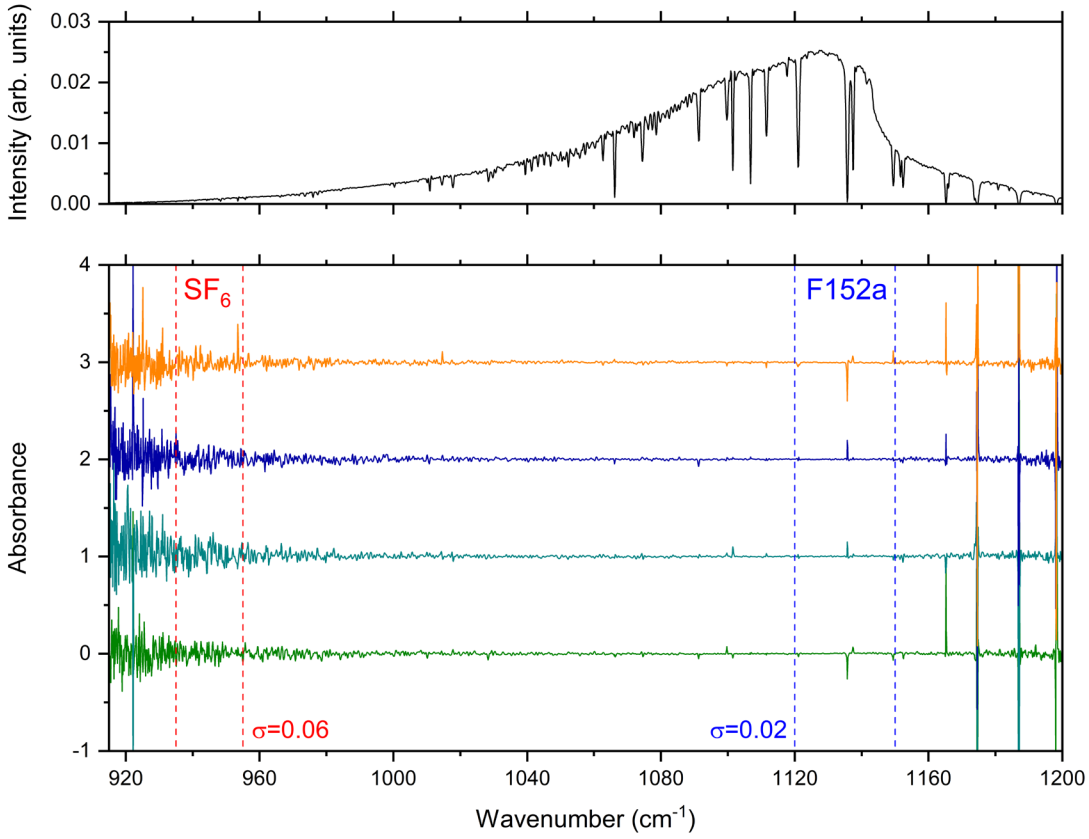

Figure 14: Scan intensity versus wavenumber (top) and series of 4 absorbance spectra (bottom) after averaging to 10 Hz rate (0.1 s per spectrum). The absorption regions for SF_6 and F152 are marked, along with the absorbance noise (standard deviation) in these windows.

Figure 15 and Figure 16 show examples of absorbance spectra for detected gases in plumes as measured by the system. Figure 15 shows an example of F152a taken from the data on 11/07 with shorter measurement path but high detected column densities. The measured data is compared with the library spectrum, and the best-fit spectrum shows a positive identification of the species. The fit residual spectrum is for the most part structureless, indicating a good match between measured and library spectra. Sharp spikes in the residual spectrum occur near regions of strong H_2O absorption, leading to corresponding high absorbance noise due to low light levels on the detector. Figure 16 shows an example of detected SF_6 in a plume on 11/04 with the longer measurement path. The higher absorbance noise is apparent in this part of the scan window, but nevertheless the SF_6 is detected with confidence.

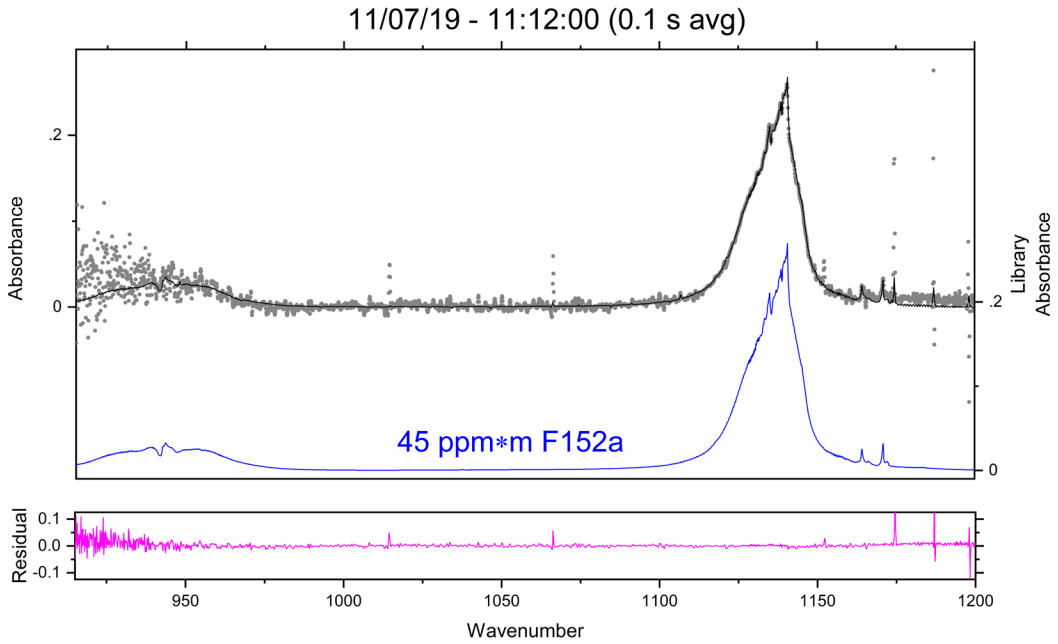

Figure 15: Example of detected F152a spectrum (grey points) and spectral fit (solid black line). The reference spectrum for F152a is also shown, scaled for the best-fit column density of 45 ppm*m. The lower panel shows the fit residuals.

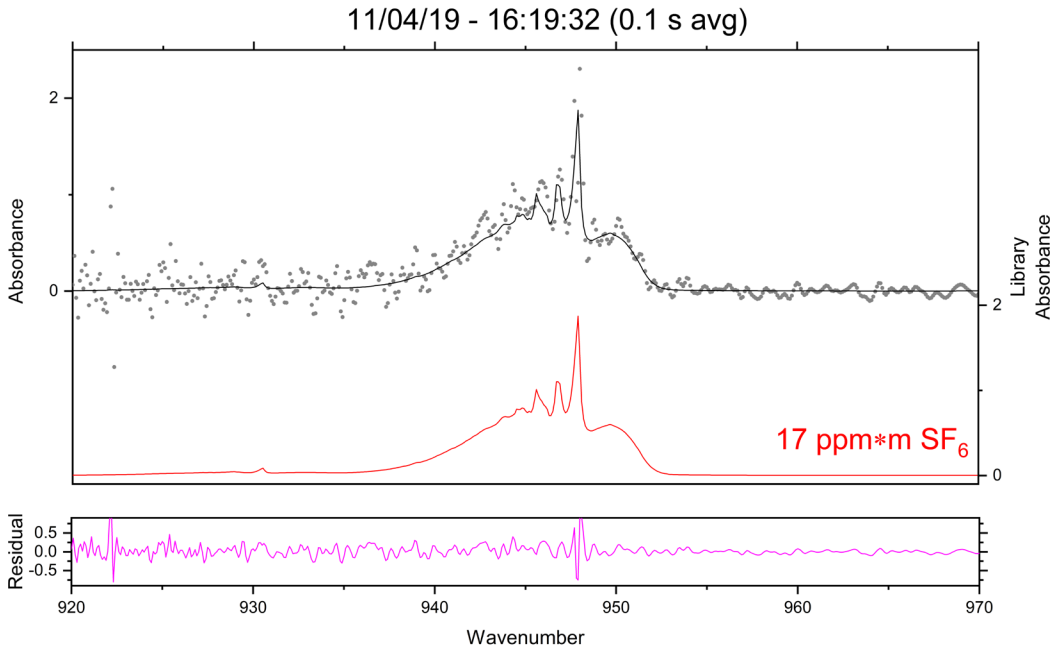

Figure 16: Example of detected SF_6 spectrum (grey points) and spectral fit (solid black line). The reference spectrum for SF_6 is also shown, scaled for the best-fit column density of 17 ppm*m. The lower panel shows the fit residuals.

The measured data after initial processing results in a time series of absorbance spectra. Figure 17(a) shows an example time-series of absorbance spectra from 11/07 when a F152a

plume passed through the measurement path. Over this 10s window, the absorption spectrum of F152a is seen to increase in magnitude and then decrease. The quantitative WLS spectral fitting analysis is performed on every absorbance spectra, and the output of the analysis is a corresponding time series of measured column densities for each species in the analysis library. Figure 17(b) shows the results of the WLS analysis for F152a column density resulting from analysis of the spectra in Figure 17(a).

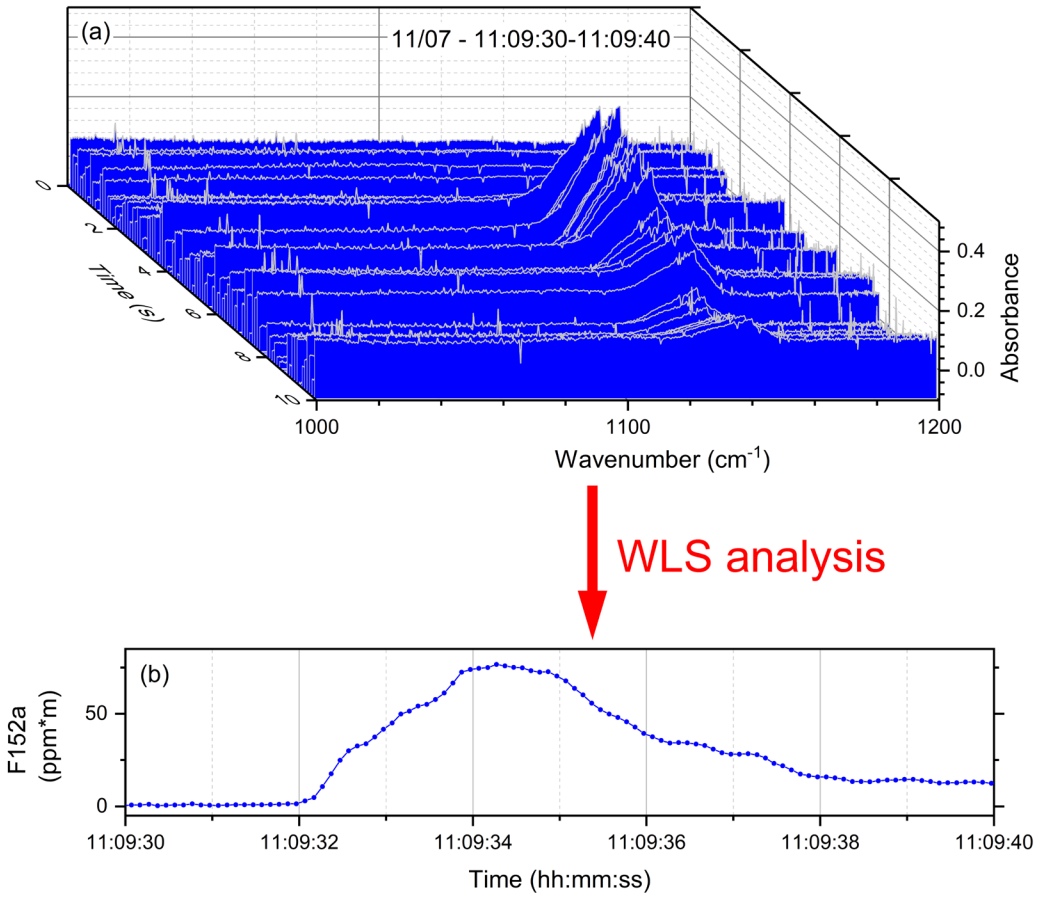

Figure 17: Example series of absorbance spectra and resulting time-series of measured column densities for F152a after WLS analysis.

5.0 Measurement Results

Data was collected in continuous segments, but not typically covering an entire day without interruption. Breaks in the data collection were made for occasional realignment of the optical mirrors to maximize the return power from the retro-reflector. Throughout the day, short datasets were acquired using the wavelength scan etalon to use for calibration of the wavenumber axis. Other breaks were made to collect data for local small F152a releases near the ECQCL system to verify system performance or for demonstrations. In total, over the 4 days of operation ~350 GB of raw data was acquired in binary format. Because the raw scan data is of little general use before analysis, it will not be delivered to the team; however, it has been saved and backed up on hard drives and is available if additional analysis needs to be performed.

For delivery of data to the team, files were formatted as ASCII text, tab-delimited files. Filenames are denoted by date, start time, and end time as follows: MMDDYY_hhmmss-hhmmss_conc.txt. Each file represents a continuous block of analyzed data. The columns, units, and descriptions are given in**Error! Reference source not found.**, with rows providing the local time at 1 s intervals. In the output files, entries marked NaN correspond to times at which the detected power was below a set threshold level and thus the analysis could not be performed. This is most common in data from 11/07/19, corresponding to times at which vehicles passed through the beam path, blocking the light from returning to the detector.

Table 5 shows a listing of all output data files.

Table 4: Output data file format

Time	CO_2	F152A	H_2O	N_2O	NH_3	PTCH	SF_6	Offset	Slope	Spectrum Mean	Integrated Power	RMS Fit Residual
hh:mm:ss.xxx	*ppm*m*	*ppm*m*	*ppm*m*	*ppm*m*	*ppm*m*	*ppm*m*	*ppm*m*	*Absorbance (unitless)*	*Absorbance (unitless)*	*Absorbance (unitless)*	*Arb. Units*	*Absorbance (unitless)*
Local time	Column density	Column density	Column density	Column density	Column density	Column density	Column density	System diagnostic	System diagnostic	System diagnostic	Spectrally-integrated return power	System diagnostic

Table 5: List of output data files

Output Data Files	
1.	110419_145125-153848_conc
2.	110419_154912-163030_conc
3.	110519_100128-100750_conc
4.	110519_101336-102523_conc
5.	110519_102809-105924_conc
6.	110519_110753-134313_conc
7.	110519_134442-142427_conc
8.	110519_142608-152749_conc
9.	110519_155112-161451_conc
10.	110619_095120-105929_conc
11.	110619_111445-130406_conc
12.	110619_130937-132135_conc
13.	110719_102838-124659_conc
14.	110719_124759-162053_conc
15.	110719_162130-162540_conc

The next sections provide a summary of the measurement results for each day of testing. Notes and comments about the results and possible interpretations are also provided. The interpretation of the results is preliminary at this time, and in the future should be compared directly against the plume release timing/locations and any local time-resolved wind measurements.

5.1 Measurement Results- 11/04/2019

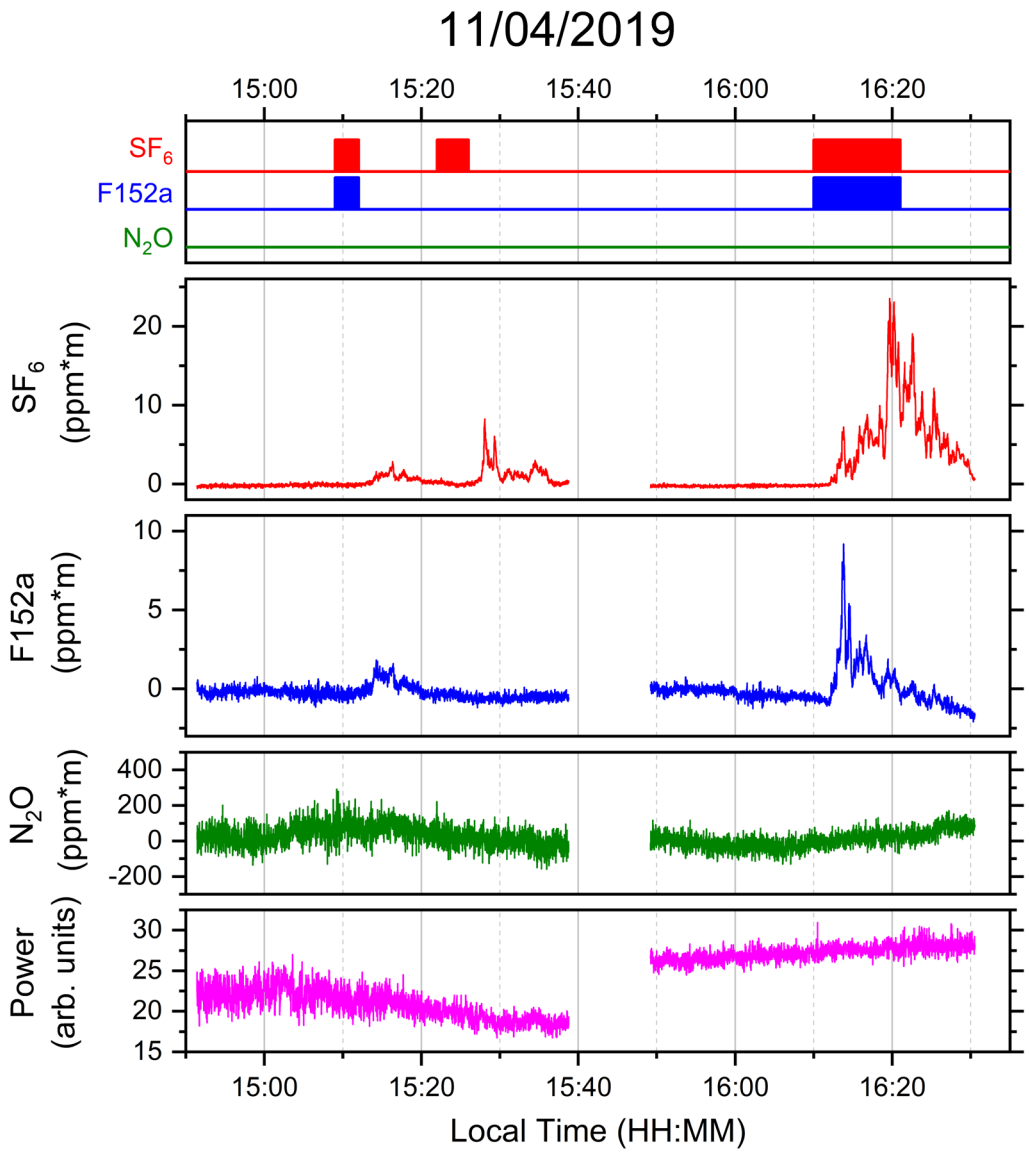

Figure 18: Measurement results from 11/04.

Figure 18 shows results from measurements obtained on 11/04/2019. The top panel shows the times at which the various chemicals were released (quantities or release rates of chemicals are not shown at this time). The release locations will be noted in discussions below. The middle panels show the measured time-resolved column density for SF_6, F152a, and N_2O throughout the day, averaged to 1 second intervals. The bottom panel shows the total power (spectrally-integrated) as a function of time throughout the day and serves as a diagnostic of system alignment and atmospheric conditions. The gap in the data from 15:40 – 15:50 corresponds to times at which the system was being aligned, wavelength calibrations were being performed, or other system adjustments were being made. For example, the higher power at 15:50 relative to 15:40 resulted from adjustments of the system mirrors to improve the optical alignment.

The column densities remain approximately near zero when no plume releases were occurring; however, slow drifts are observed during the day. Drifts typically result from small optical alignment changes in the system, temperature fluctuations, changes in detector responsivity, or other variations in electronic components. The data was processed by using a single background spectrum obtained at the beginning of each day; therefore, all column densities start at zero. Slow drifts resulting throughout the day were thus not removed from the data as presented and should not be misinterpreted as actual changes in column density. If desired, the remaining drifts could be accounted for by using additional background spectra at later times in the day to re-normalize the column densities to zero periodically.

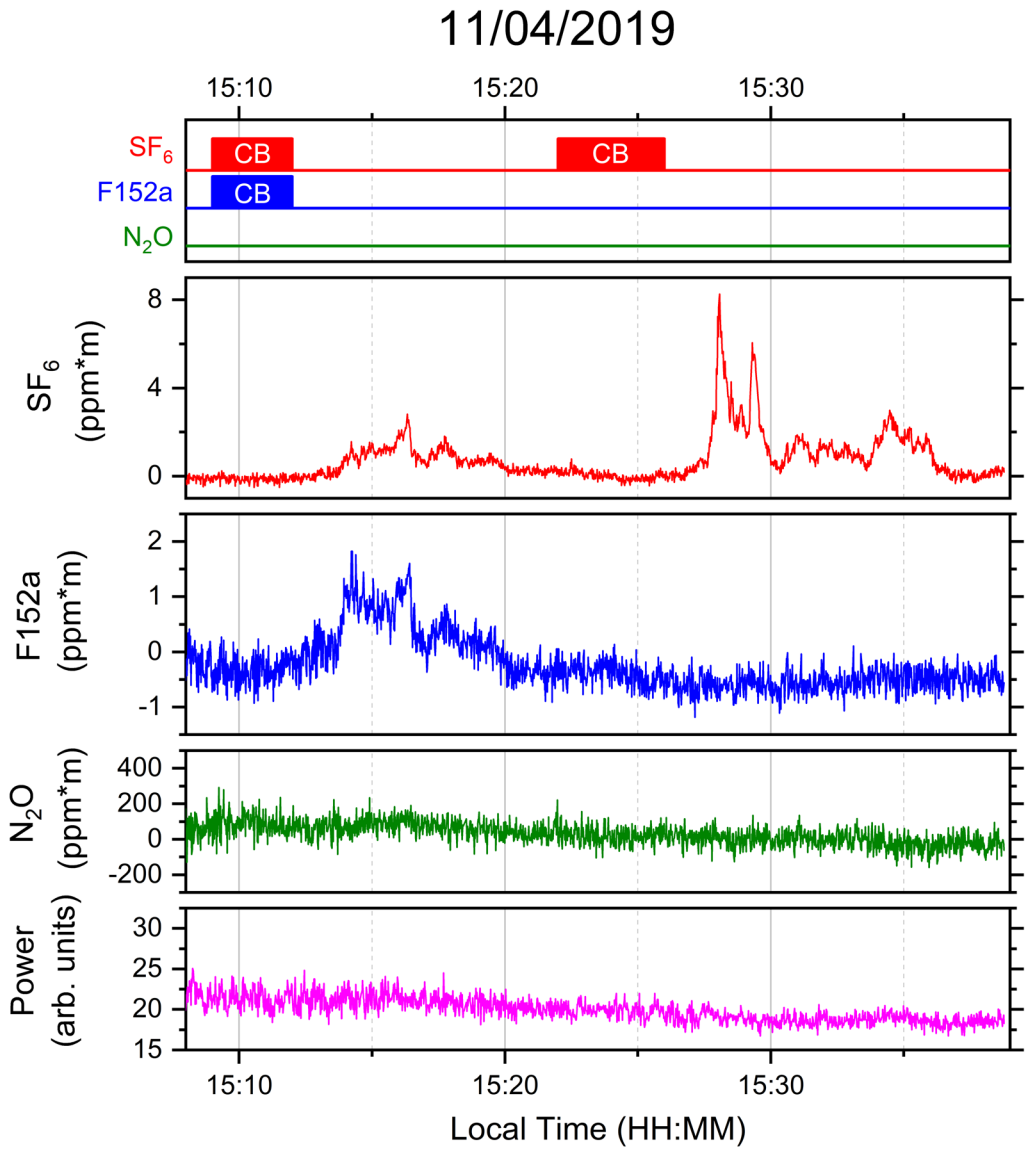

Figure 19: Measurement results from 15:10-15:40 on 11/04.

Figure 19 shows a more detailed view of results from the first set of plume releases on 11/04/2019. From 15:09-15:12, SF_6 and F152a were released simultaneously from site CB. After a short delay, a rise in detected column density was detected for both SF_6 and F152a,

indicating presence of both chemicals along the measurement path. The delay in detection results from the plume propagation from the release point to the measurement path. The overall duration of detection was similar for both SF_6 and F152a, persisting from ~15:14-15:25, as expected given that the chemicals were released from the same location. The change in column density was higher for SF_6 than for F152a. This may indicate that a larger mass of SF_6 was released, but this needs to be verified. The SNR is higher for SF_6 than for F152a due to the higher absorption cross-section of SF_6.

From 15:22-15:26, only SF_6 was released from site CB. In this case, only SF_6 was detected by the swept-ECQCL. No change in F152 column density is visible above the noise floor, as expected, thus verifying the ability of the system to differentiate SF_6 and F152a. The SF_6 plume was detected at the measurement path from ~15:25-15:40, with a time dependence likely resulting from the complex local topography and winds.

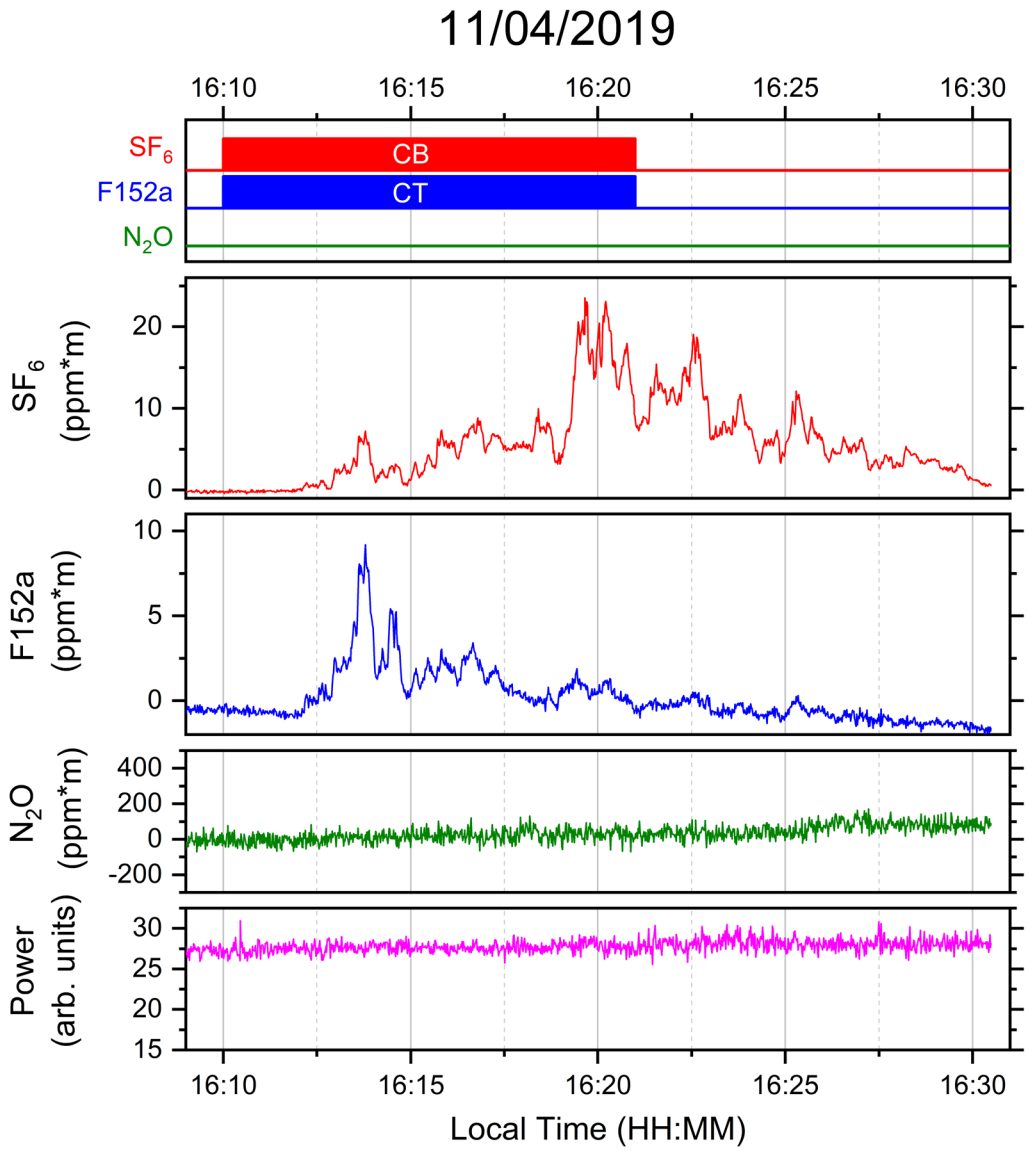

Figure 20: Measurement results from 16:10-16:30 on 11/04.

Figure 20 shows a detailed view of results from the second set of plume releases on 11/04/2019. SF_6 and F152a were released simultaneously from 16:10-16:21 (need to verify times); however, the SF_6 was released from site CB and F152a was released from site CT. The different release locations result in different time-dependence of the detected column density. The plume arrival times were similar for both chemicals at the measurement location, occurring at ~16:12. Both plumes were detected from ~16:12-16:30; however, it appears both were still being detected after the system was shut down for the day at 16:30. The F152a shows large peaks at ~16:14-16:15, followed by a period of smaller signals from ~16:15-16:30. The SF_6 shows a slower rise in signal, peaking between ~16:19-16:22 before decaying. The differences in time-dependence observed between SF_6 and F152a may be interesting with respect to plume propagation dynamics through complex terrain.

5.2 Measurement Results- 11/05/2019

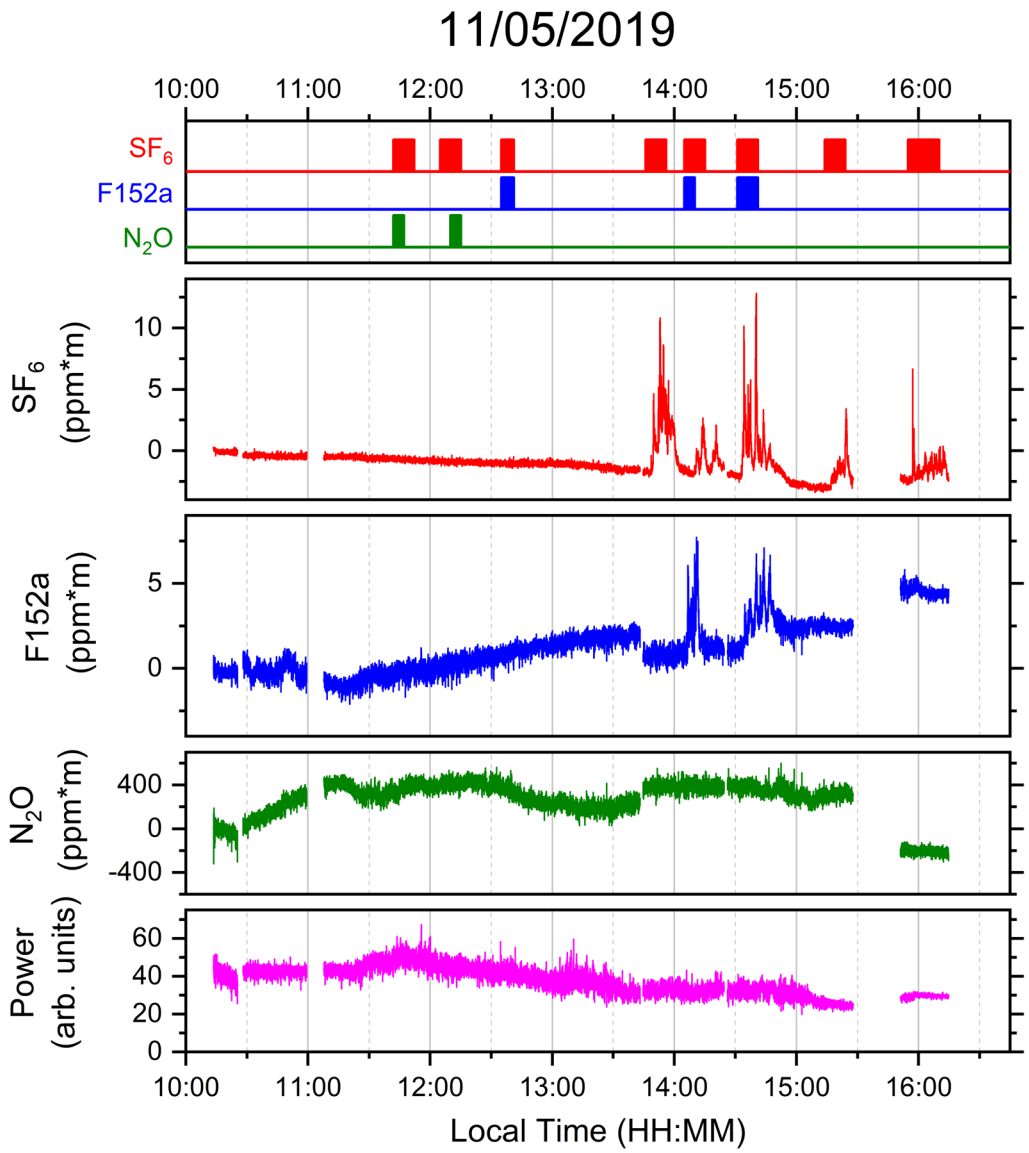

Figure 21: Measurement results from 11/05.

Figure 21 shows results from measurements performed on 11/05/2019. Long-term drifts in signal levels are more apparent; however, these do not interfere with the ability to detect the transient changes due to the plumes. The set of plume releases which occurred before 13:00 were not detected by the ECQCL, presumably because the release locations were downwind of the measurement path. Additional information is needed on the local wind conditions during these time periods. [Note: there is some uncertainty in the plume release times/locations on 11/05 as indicated in the main report].

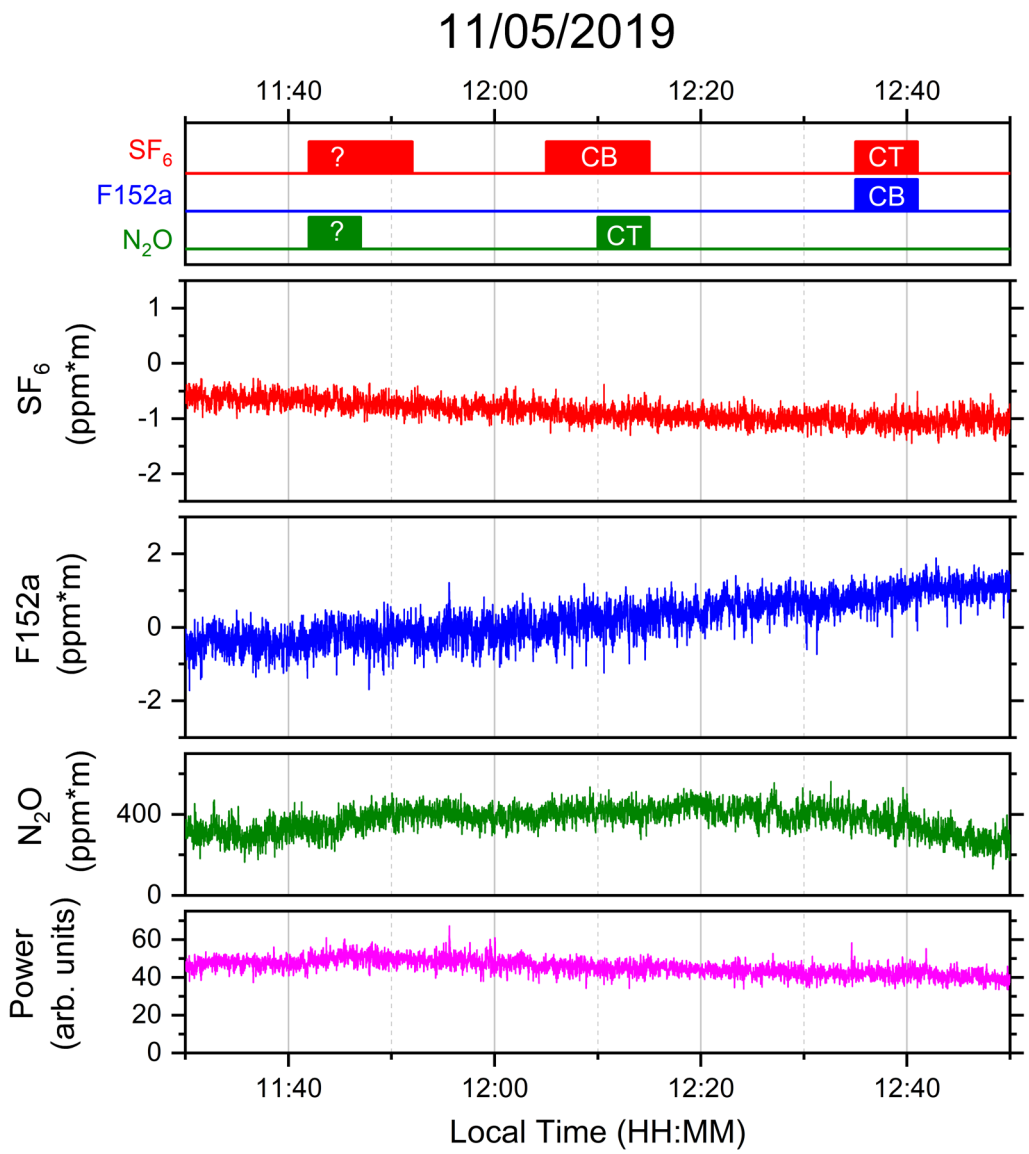

Figure 22: Measurement results from 11:35-12:45 on 11/05.

Figure 22 shows a detail of the measurements from the first set of chemical releases. For these releases, the chemicals were released from either the CB or the CT sites; however, no plumes were detected at the location of the ECQCL measurement path. Assuming the wind data is available, the lack of detections should be consistent with the plume moving away from the measurement path.

It is worth noting that although visible, the actual drift in column density over this hour-long time period is very small, especially for a continuous laser-based sensing technique. While it is most likely that the drifts are the result of small changes in instrument alignment, it is also possible that the apparent drifts result from small and slow variations in the gases along the measurement path. For reference, a 1 ppm*m variation in column density corresponds to a 300 ppt (part-per-trillion) variation in concentration when integrated over the full 3000 m measurement path. Therefore, it is certainly possible that some of the gases may build up slowly in the measurement region, or slowly disperse.

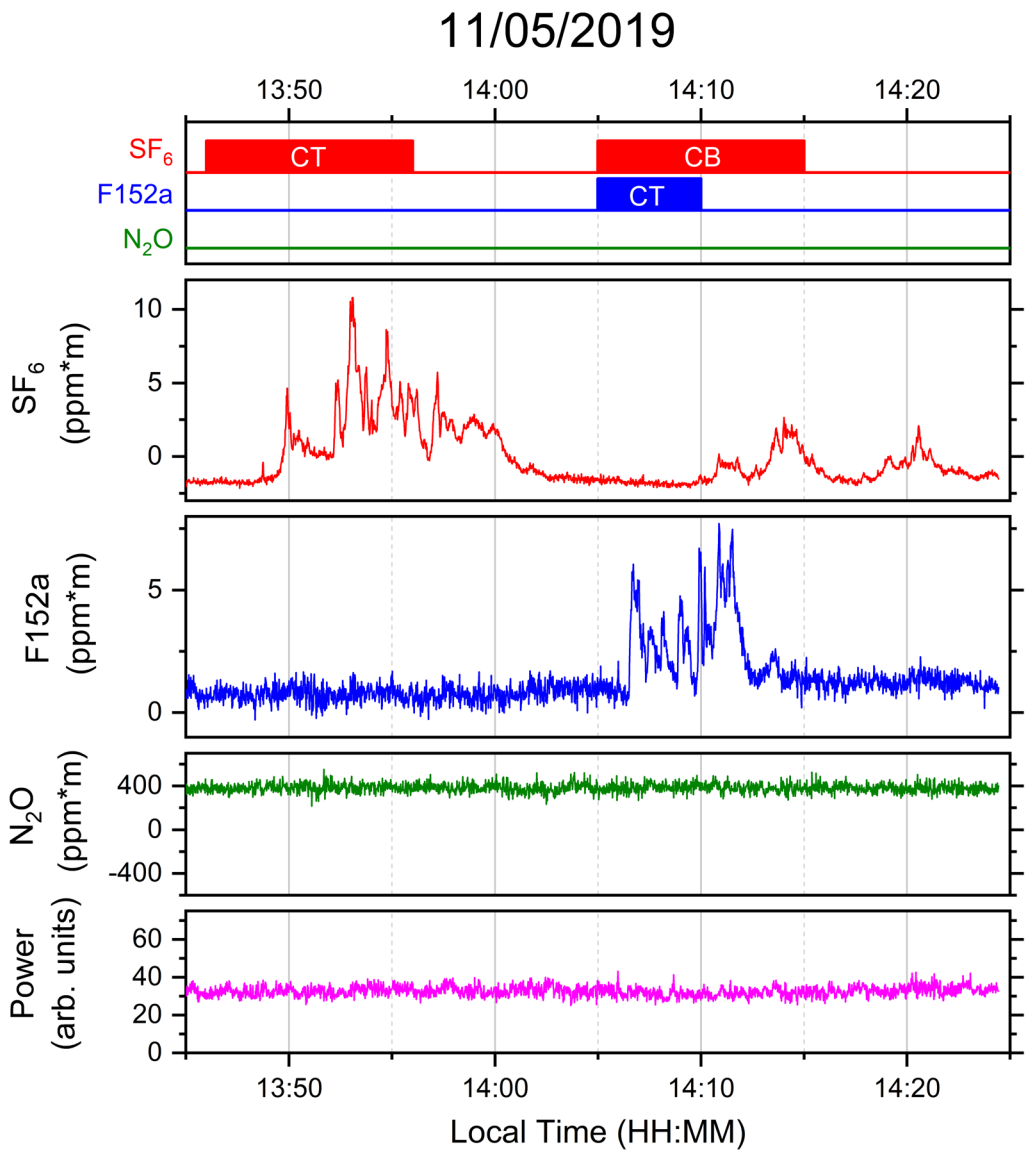

Figure 23: Measurement results from 13:45-14:25 on 11/05.

Figure 23 shows details of the second set of releases occurring on 11/05. The first release was SF_6 from 13:46-13:56 at the CB site. In this case, the SF_6 was detected from ~13:49-14:11, indicating a plume with negligible temporal spread (i.e., the duration of plume detection was similar to the duration of the release). This behavior may indicate the presence of steady winds (need to confirm). The second release consisted of SF_6 from 14:05-14:15 from the CB site, and F152a from 14:05-14:10 from the CT site. In this case the dynamics of the detected plume signal are clearly different, as a result of the different release durations and locations. The F152a was detected first, and from ~14:06-14:15. The SF_6 was not detected until 14:10 but then was detected over a longer duration from ~14:10-14:25.

According to the release notes, 3 cans of F152a were released in total, which corresponds to ~850 g of gas assuming the cans were emptied completely. Using the molecular weight of F152a (1,1-difluorethane) as 66 g/mol, this mass corresponds to 12.9 moles of F152a. If the F152a filled a sphere with 100 m diameter uniformly, the concentration would be 6 ppb (by volume). If the plume intersected the measurement path over a length of 100 m, then the

detected column density would be 6 ppb * 100m *2 = 1.2 ppm*m. The peak detected column densities for F152a in the release were ~5 ppm*m, which is of the same order of magnitude. Despite the crude calculation, the results are reasonable. A more detailed plume propagation model would be very useful for comparison.

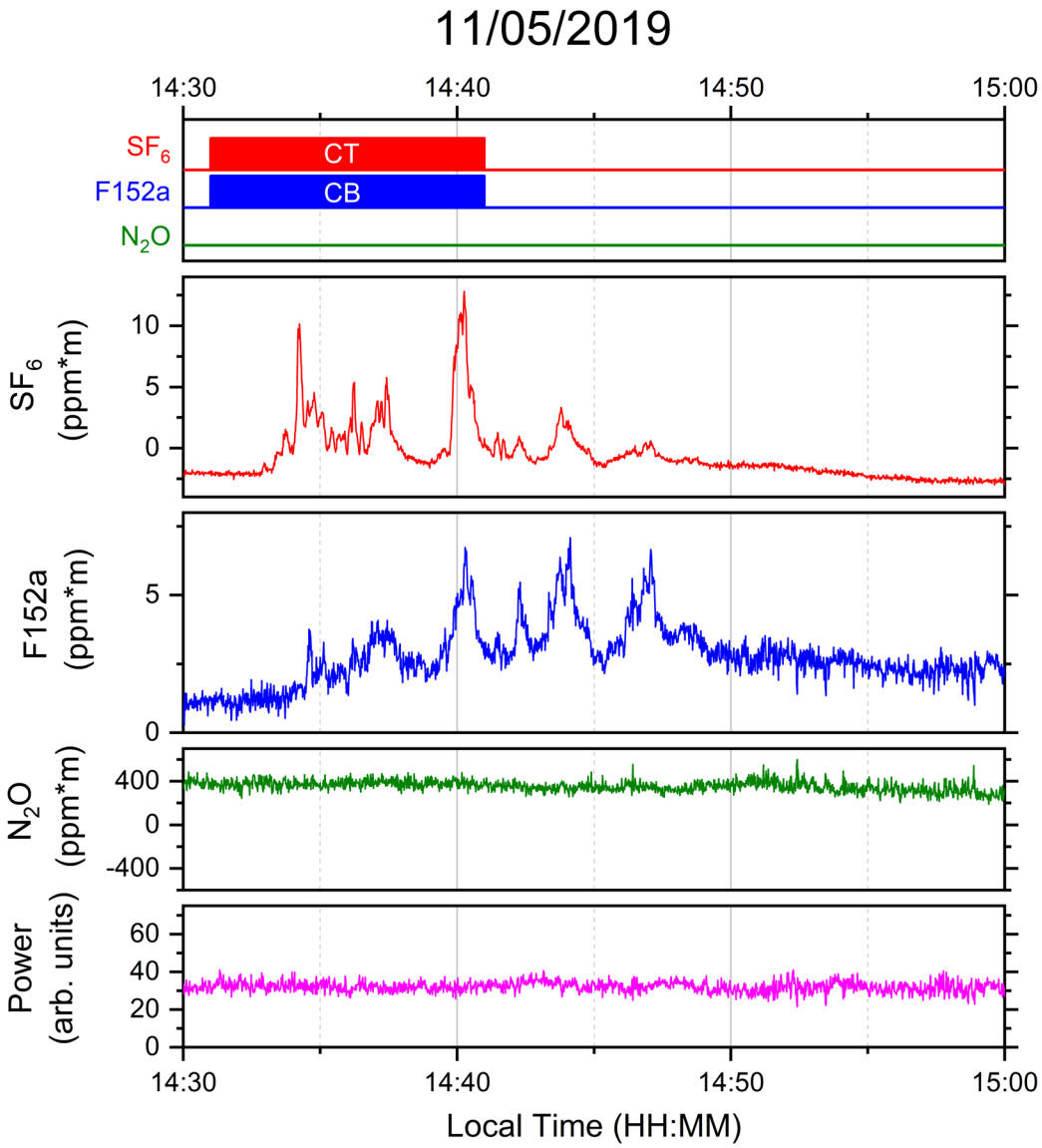

Figure 24. Measurement results from 14:30-15:00 on 11/05.

Figure 24 shows a detail of the measurement results from 14:30-15:00 on 11/05. In this case, both F152a and SF_6 were released from 14:31-14:41 (need to verify), with F152a from CT site and SF_6 from CB site. In this case, the dynamics of the detected column densities were qualitatively similar. Most notable is the extended detection time of both gases from ~14:33-14:55, indicating some degree of plume extension in time relative to the release duration. This may have resulted from lower wind speed or variable wind direction.

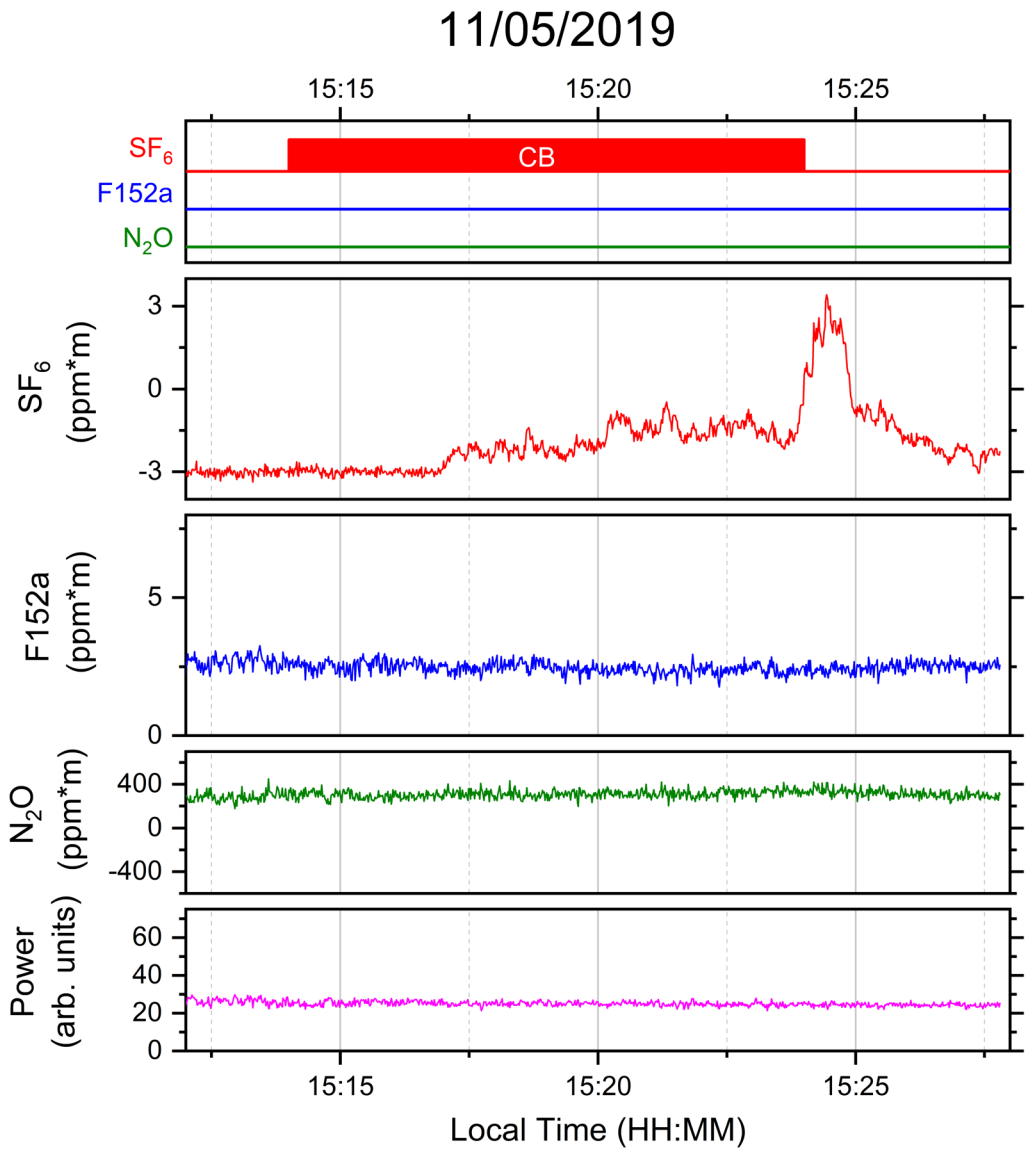

Figure 25. Measurement results from 15:12-15:28 on 11/05.

Figure 25 shows measurement results from 15:12-15:28 on 11/05. SF_6 was released from 15:14-15:24 from CB site. The SF_6 was detected at the measurement path at ~15:17, indicating a ~3-minute delay between release start and first detection. The time of detection was ~15:17-15:27, which is of similar duration to the release.

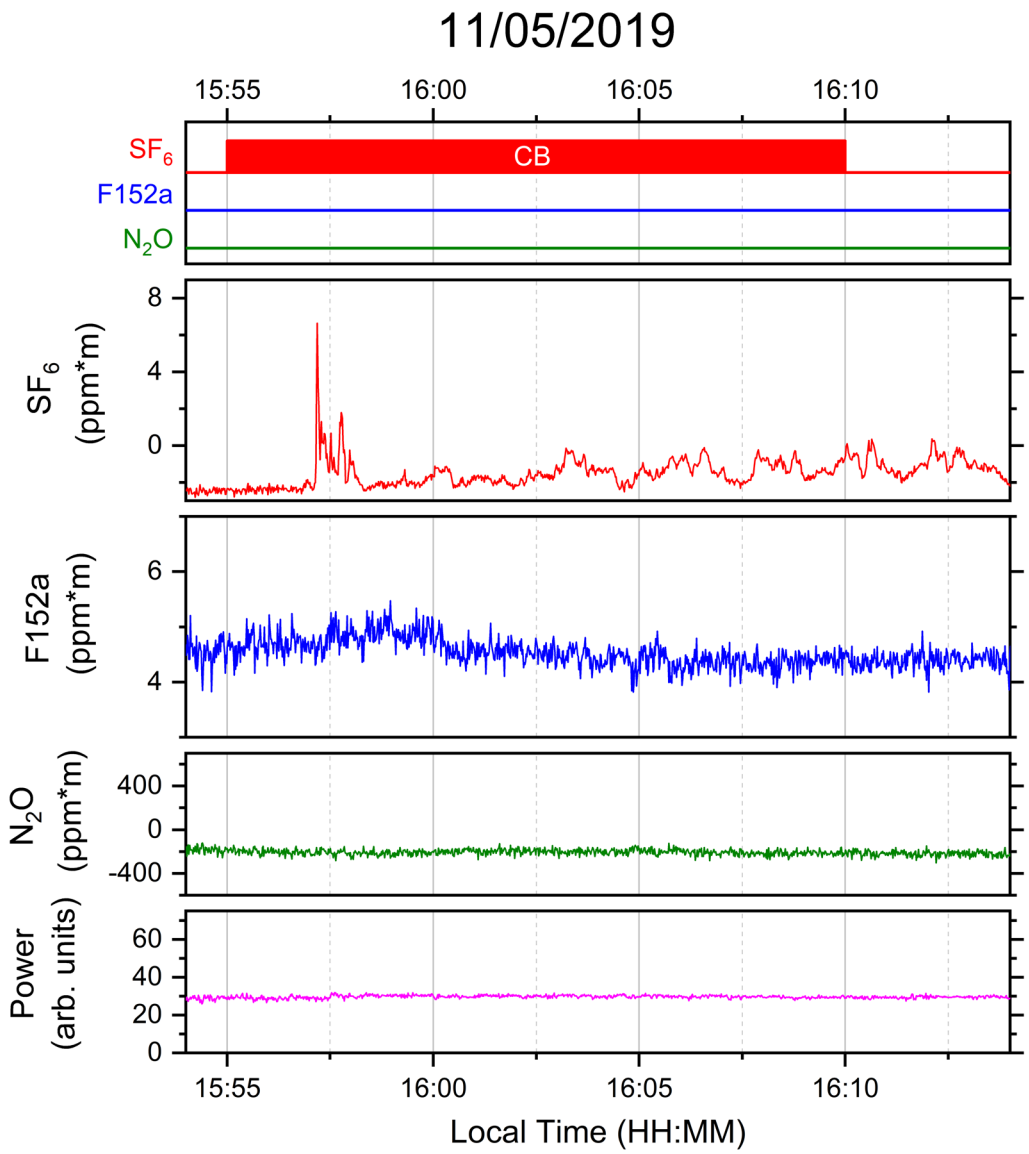

Figure 26. Measurement results from 15:55-16:15 on 11/05.

Figure 26 shows measurement results from the last release on 11/05. SF_6 was released from 15:55-16:10 from CB site. SF_6 was detected starting at ~15:57 and continuing past 16:14, when the system was shut down for the day. The dynamics of detected signal are interesting, consisting of a large initial set of spikes with high column density, followed by a longer region of lower column density. This may reflect variations in release rate, or variations in wind speed/direction during the release times.

5.3 Measurement Results- 11/06/2019

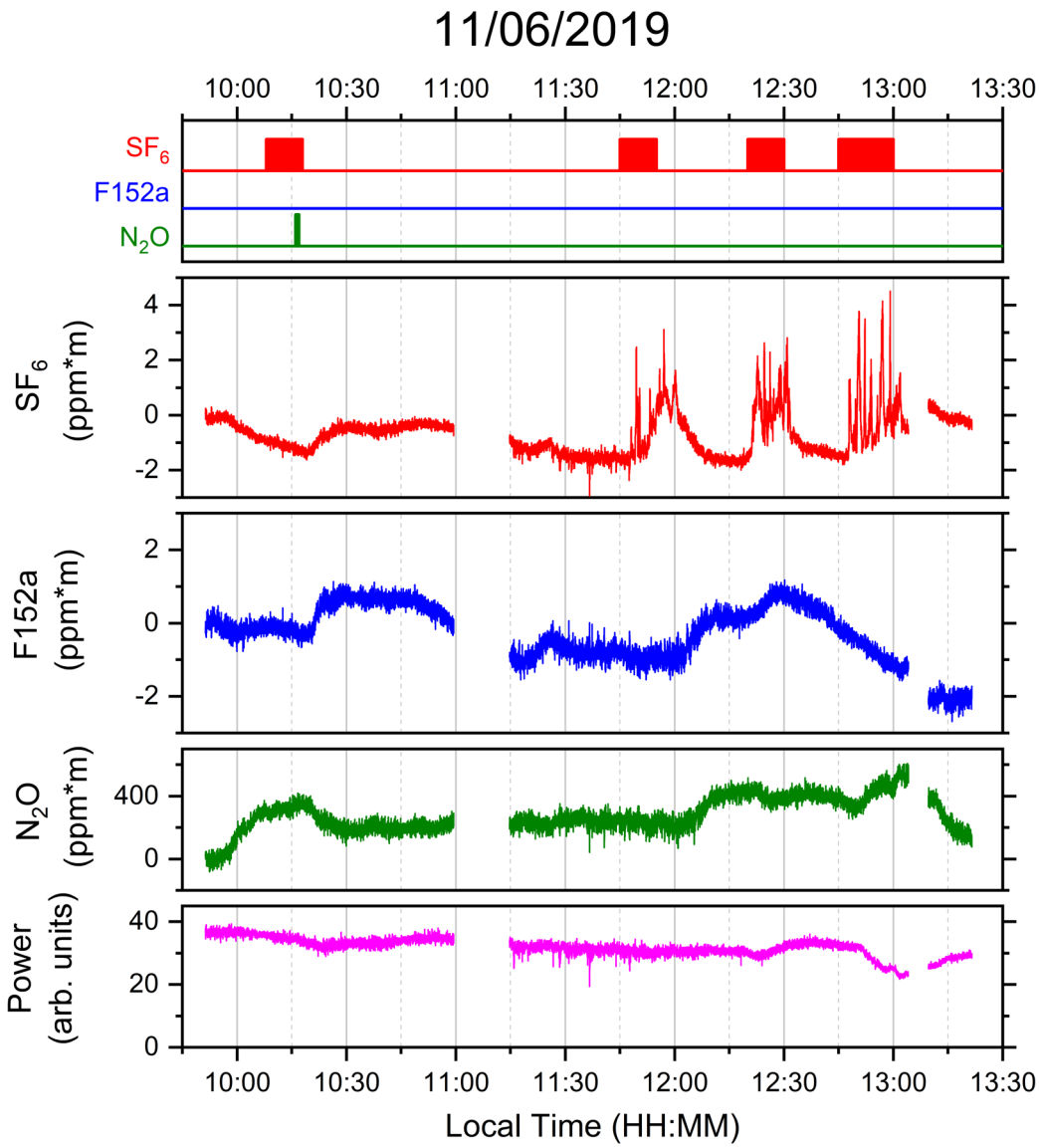

Figure 27: Measurement results from 11/06.

Figure 27 shows results from measurements on 11/06. The system was powered on at 09:40 am and it was noted that the optical alignment to the retroreflector was preserved overnight, with only minimal optimization of mirror angles required. Light rain was present at various times throughout the day; however, the system still operated during these conditions. The main effect of the rain was to attenuate the return beam signal, as can be seen in the times between ~11:15-12:00 in Figure 27. A corresponding increase in noise is observed for the SF_6, F152a, and N_2O signals at these times. Heaver rain would presumably lead to larger signal attenuation, eventually leading to zero return signal. Nevertheless, it is noteworthy that operation is possible in these light rain conditions, at a standoff distance of 1.5 km.

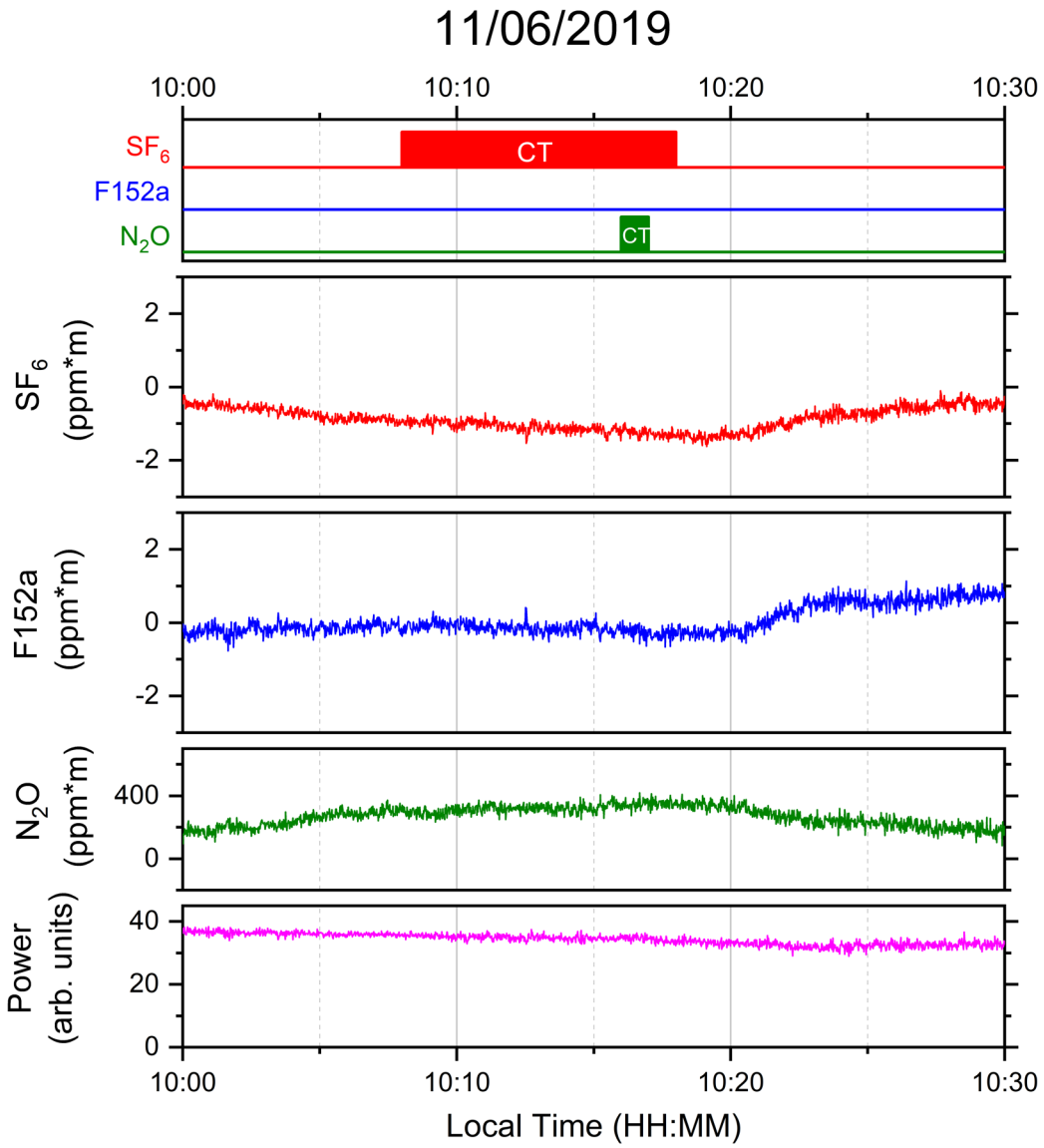

Figure 28: Measurement results from 10:00-10:30 on 11/06.

Figure 28 shows measurement results from the first release on 11/06. SF_6 was released from 10:08-10:18 from location CT, with an increased release rate occurring from 10:13-10:18. N_2O was also released from CT from 10:16-10:17. No signals were detected with the ECQCL system during this release, presumably due to wind conditions propagating the plume away

from the measurement path. This data should be compared with wind data from these times to confirm.

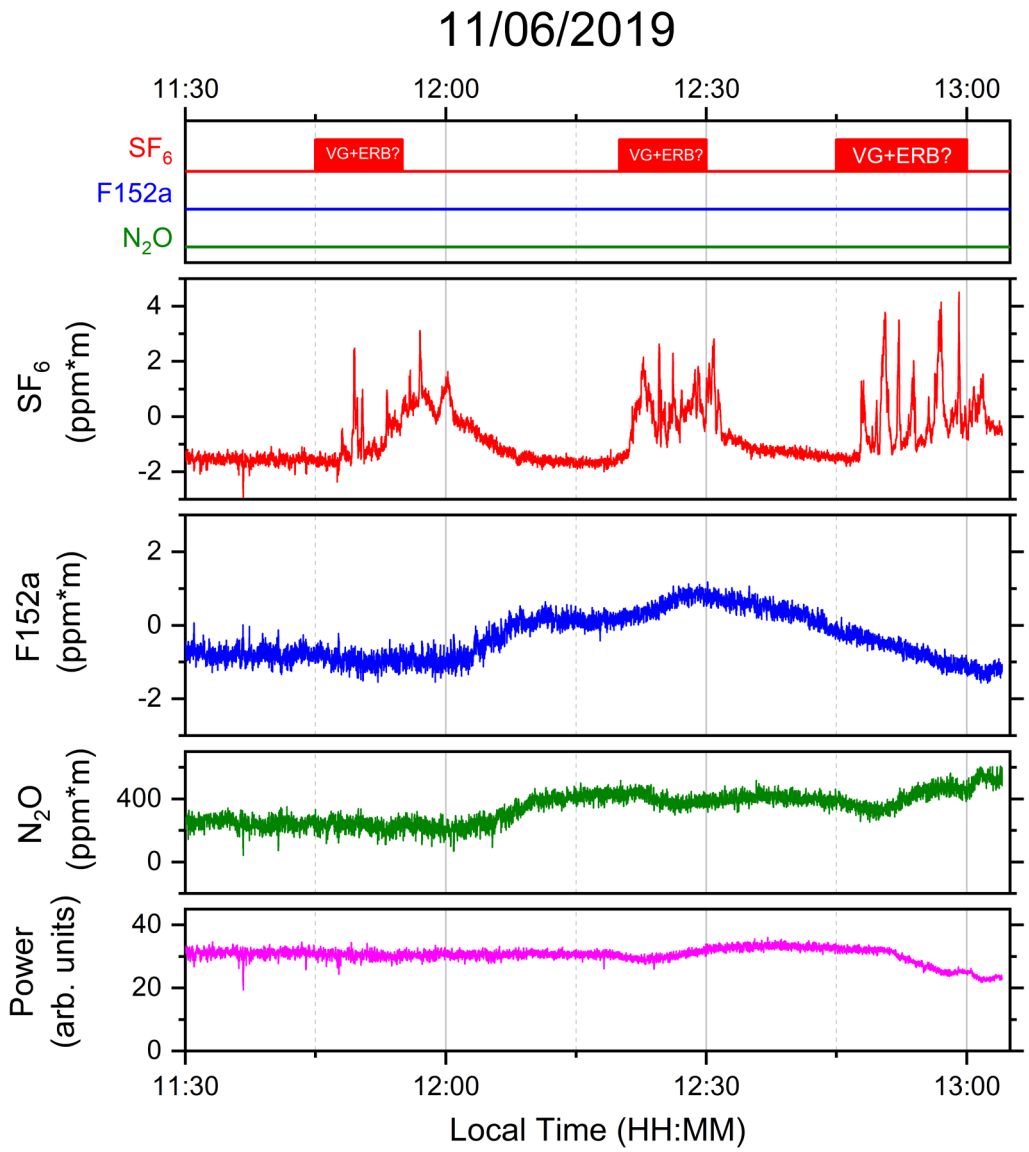

Figure 29: Measurement results from 11:30-13:00 on 11/06.

Figure 29 shows measurement results for a series of 3 plume releases over the time period 11:30-13:00. The release notes indicate that SF_6 was released from the VG location for each case, and possibly also from the ERB location (results need to be confirmed). In all 3 releases, the SF_6 was detected at the ECQCL path soon after the release was started and continuing throughout the duration of the release. SF_6 continued to be detected after each release was stopped, with a slow decay possibly indicating the SF_6 persisted in some region in or upwind of the measurement path. The measurement dynamics with multiple time scales during each release may be interesting when correlated with local wind conditions and topography. Figure 30 shows additional detail on the temporal dynamics of measurements for the third release. It may be worthwhile to plot the results for this release at a higher 10 Hz rate, given the faster dynamics of the signals.

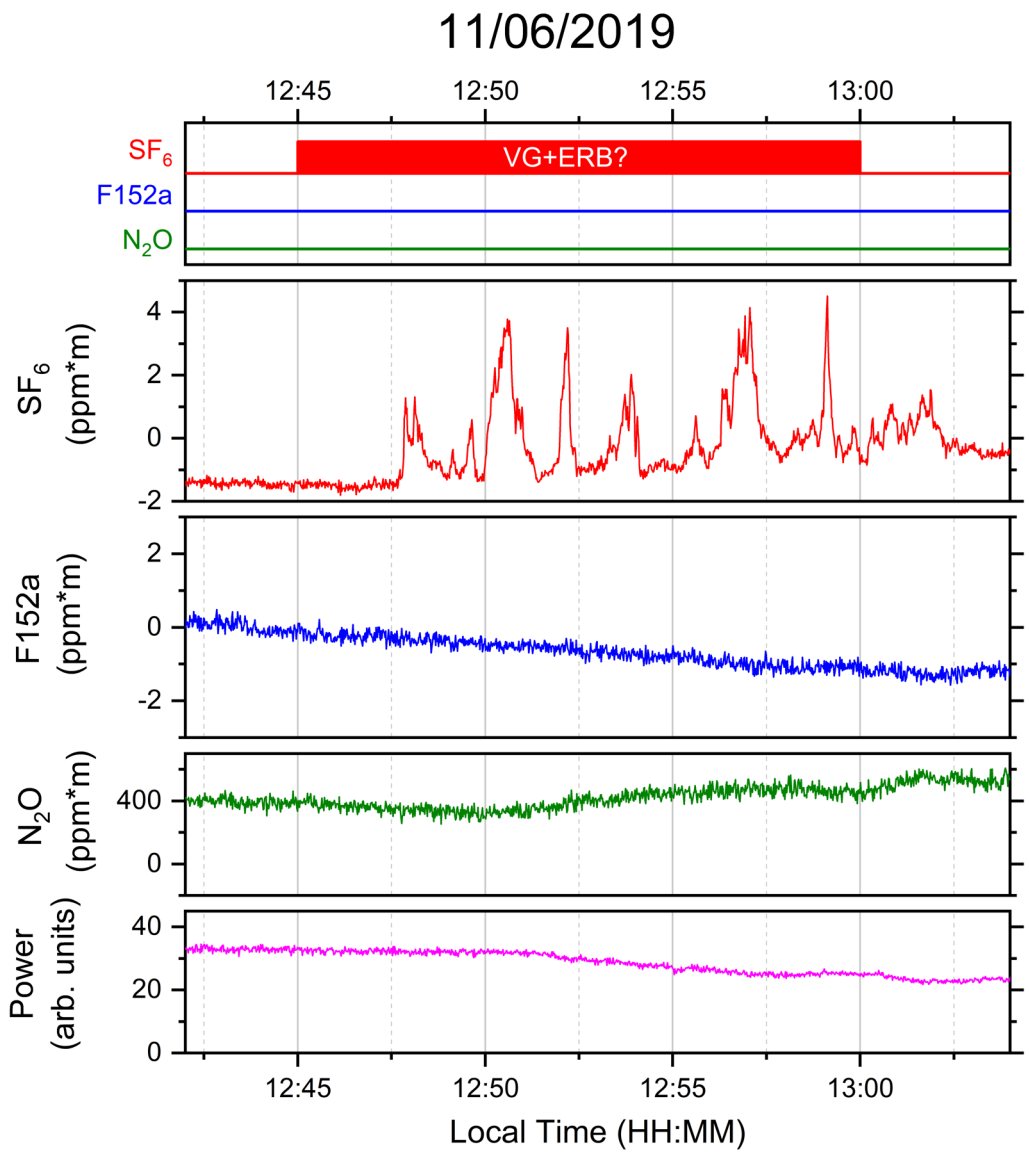

Figure 30: Measurement results from 12:43-13:03 on 11/06.

6.0 Summary and Conclusions

Overall, the swept-ECQCL system operated as expected during the measurement campaign and acquired large amounts of data over most of the testing days. The timing of the detected column densities at the measurement path should provide valuable data for comparison with wind data and plume propagation models. The results clearly show complex time-dependence due to the local terrain and local winds. Differences in detected column densities were observed when the tracer chemicals were released from different locations, and in some cases when the tracers were released from the same location.

Further analysis of the measurement data is required before drawing any major conclusions regarding the goal of the overall test campaign. It will be interesting to correlate the measured time-resolved column densities with the local wind speed and direction data, if available. It will also be very interesting to compare the measured column densities with any plume propagation model outputs. Finally, the measured column densities can be compared with the Telops measurements from the co-located instrument. In this case, it may be possible to use the ECQCL measured column densities as "ground-truth" for the Telops hyperspectral data.

The lack of N_2O detections was expected based on the low absorption cross-section. It is interesting to note that in all cases when N_2O was released, SF_6 was also released. However, no SF_6 was detected for these releases, indicating that the wind direction propagated the plumes away from the measurement path. Therefore, we cannot conclude that the N_2O plumes could not have be detected if the wind direction was different. Nevertheless, N_2O is not an ideal tracer selection due to its low absorption cross-section in the LWIR. In the MWIR, although the absorption cross-section is higher, the 300 ppb ambient concentration leads to significant background absorption even in the absence of the plume, which is not an ideal situation for tracer detection experiments.

From an operational perspective, the system showed a successful demonstration of remote plume detection at the longest standoff distance attempted to date – 1.5 km. Initial alignment of the ECQCL beam to the retro-reflector was challenging, partly due to the limited magnification available from the visible alignment camera. There are plans to upgrade the visible alignment system in the future, as discussed in 6.0Appendix B, which are expected to make initial alignment easier and faster. Once the initial alignment was performed, the system maintained its optical alignment over the 3 days of testing.

For future tests, it would be highly beneficial to acquire reference data over a full day onsite without plume releases to enable better characterization of system noise and drifts. The system should also be operated continuously if possible, even in times where no plume releases are scheduled and for longer times after plume releases have ceased. System modifications to allow autonomous operation would be beneficial, such as integrating an automatic optical alignment system to maintain the maximum return signal from the retro-reflector at all times.

Appendix A – Noise and Sensitivity

This section includes an analysis of the system noise and the resulting measurement sensitivity for the different tracer gases and other chemicals.

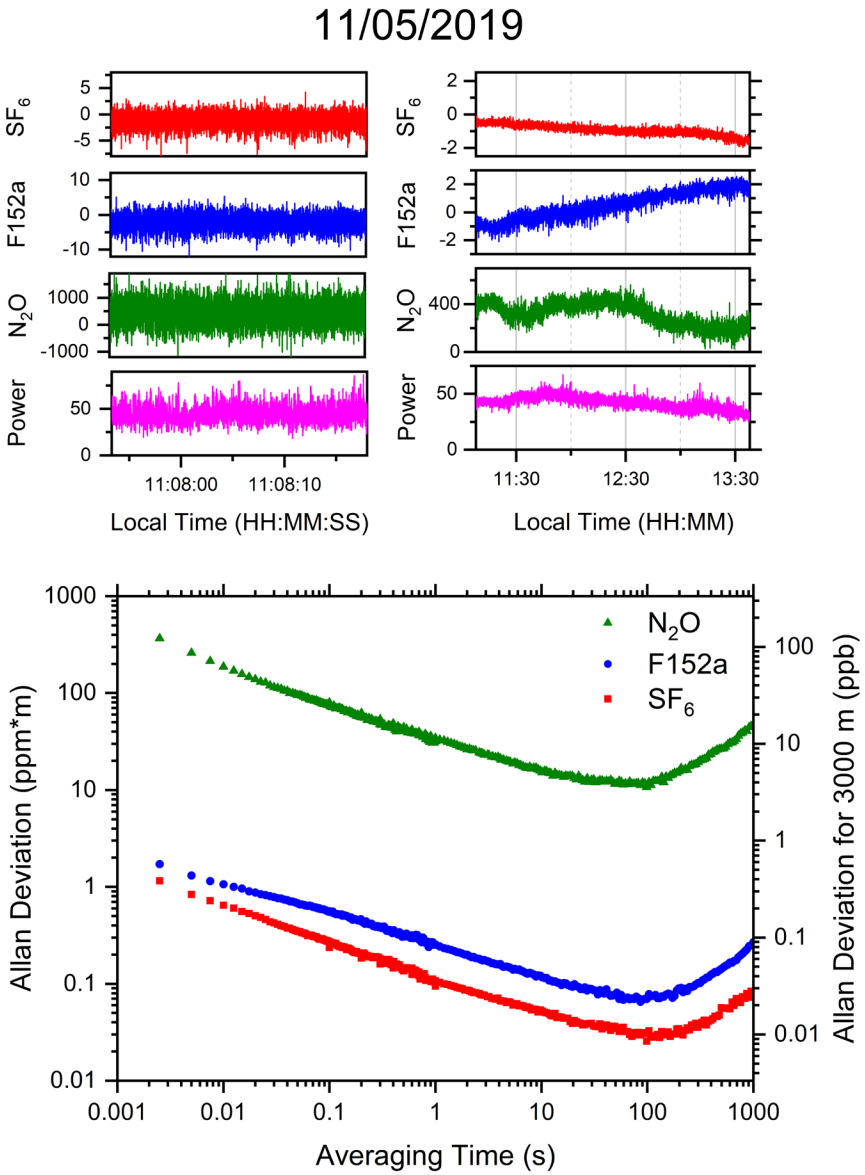

Figure 31: Allan deviation analysis of data from 11/05 to determine measurement noise as function of averaging time. The top panels show the time-series of data used in the analysis, plotted on two different time scales. The bottom plot shows the results of the Allan deviation, with noise-equivalent column density shown on the left axis, and noise-equivalent concentration assuming uniform concentration along the measurement path shown on the right axis.

Figure 31 shows results from an Allan-Werle analysis on a subset of data obtained on 11/05 during which no plumes were detected. In this case, the measurement results are expected to be zero apart from system noise and drifts; thus, the statistics of the actual measurement results provide a characterization of the noise/drifts in the measurement system. The top panels show

the time-resolved measurement data used for the Allan deviation analysis. The left panels show data measured with a 400 Hz rate (2.5 ms interval between scans); a set of 80,000 measurements over 200 s were analyzed (11:07:53-11:11:13) to provide the Allan deviation up to 1 s averaging time. The right panels show data with spectra pre-averaged to 10 Hz (0.1s interval between scans); a data set consisting of 90,000 measurements over 9000 s was analyzed (11:07:53-13:37:54) to provide the Allan deviation out to longer times up to 1000 s. The lower plot shows the Allan deviation. The two analyses overlapped between 0.1-1s, where they are seen to be equal within small variations due to statistical differences between the two data sets.

The Allan-Werle analysis provides a measure of detection limit expressed as a noise-equivalent column density (NECD) for each species, depending on the averaging time. For the measurements as performed, the detection limits improve with averaging up to 100 s. For averaging times longer than 100 s, slow drifts in the measurement lead to a degradation in detection limits. The 100 s timescale for drift in measurement results is seen in the tendency of the measured column densities to vary over time scales of several minutes. The timescales of noise and drift are critical parameters for transient plume detection. For example, it is easy to distinguish the fast changes in column density occurring with ~1 s time scale as a plume intersects the beam path from instrumental drifts occurring with >100 s time scales.

Table 6 summarizes the results from the Allan-Werle analysis at various averaging times. The NECD for SF_6 and F152a are 1-2 ppm*m at 2.5 ms averaging time. Although measurements at such a fast speed was not necessary for the EMRTC experiments, other situations may benefit from a high measurement rate such as measurements of species generated in or from explosive events. For the EMRTC plume measurements, it was found that a 1s averaging time was a good match for the time scales of the plume fluctuations, while reducing the NECD to 0.1-0.3 ppm*m for SF_6 and F152a.

Table 6: Noise equivalent column density (NECD) determined from Allan-Werle analysis for the three detected species and also NH_3 at various averaging times. The last column shows the predicted noise-equivalent concentration (NEC) if the species fills the 3000 m measurement path completely and uniformly.

Species	**Plume NECD (ppm*m)**	**Plume NECD (ppm*m)**	**Plume NECD (ppm*m)**	**Full path NEC (ppb)**	**Full path NEC (ppb)**
	2.5 ms	***100 ms***	***1 s***	***10 s***	***100 s***
SF_6	1.2	0.24	0.11	0.02	0.01
F152a	1.7	0.56	0.25	0.04	0.02
N_2O	370	80	34	5	3.5
NH_3	3.0	0.53	0.22	0.03	0.03

Typical measured peak column densities for SF_6 and F152a plumes were 5-10 ppm*m, which are easily visible above the 0.1-0.2 ppm*m NECD at 1 s averaging time. The NECD for N_2O is > 300x higher than SF_6 due to the low absorption cross-section of N_2O in this spectral region. If we assume the N_2O plume has similar properties to a SF_6 plume, a 10 ppm*m column density

N_2O plume would not have been detectable above the 34 ppm*m NECD for N_2O at 1 s averaging time.

For the measurements at EMRTC, the plumes did not fill the entire measurement path due to the measurement geometry. Instead, the plumes likely filled < 10% of the path. If the ECQCL path could have been placed farther downwind of the release points, it is possible that larger fractions could have been filled by the plumes; however, the local topography will also have an influence.

The Allan-Werle analysis results can also be used to predict the detection limits for species distributed over the entire 3000 m measurement path, such as for detection of large plumes at long distances from the release point. In this measurement scenario, we predict that SF_6 variations > 10 ppt (part-per-trillion) could in principle be detected above the noise levels when using 100 s averaging times. However, we note that differentiating these variations from instrument drifts becomes more and more challenging as averaging times increase.

It is also interesting to compare the EMRTC measurement results at 1.5 km standoff distance with previous measurements using the system at 235 m standoff distance [1]. The NECD values for F152a, N_2O, and NH_3 are ~2-4x higher for the EMRTC measurements than for the previous measurements. This is not surprising given that the longer measurement path results in lower return power and larger beam deviations due to turbulence. We expect that modifying the system to use a larger beam collection aperture would improve the NECD for the longer measurement path. Despite the higher NECD with the longer measurement path, the full-path NEC is still lower for the EMRTC measurements due to the longer path length.

Table 7: Results from prior ECQCL measurements using 235 m standoff distance [1].

Species	**Plume NECD (ppm*m)**	**Plume NECD (ppm*m)**	**Full path NEC (ppb)**
	2.5 ms	***100 ms***	***10 s***
F152a	0.96	0.19	0.062
N_2O	191	36	14
NH_3	0.75	0.12	0.13

Appendix B – System Modifications Performed Before Tests

The previous swept-ECQCL standoff detection system was described in [1], where it was used for plume detection with a standoff distance of 235 m. Figure 32 shows photographs of the previous system used for standoff detection. While the system performed adequately and had also been used for standoff detection at distances up to 850 m, several potential improvements had been identified during these past experiments. Some of the issues identified with the prior system were:

1. Large mast for steering mirrors required disassembly before transport, and on-site assembly and alignment
2. Metal stand was unstable, adding difficulty to system alignment.
3. Visible alignment camera required on-site optical alignment, adding set-up time
4. Initial on-site unpacking, assembly, and alignment of the system was time-consuming

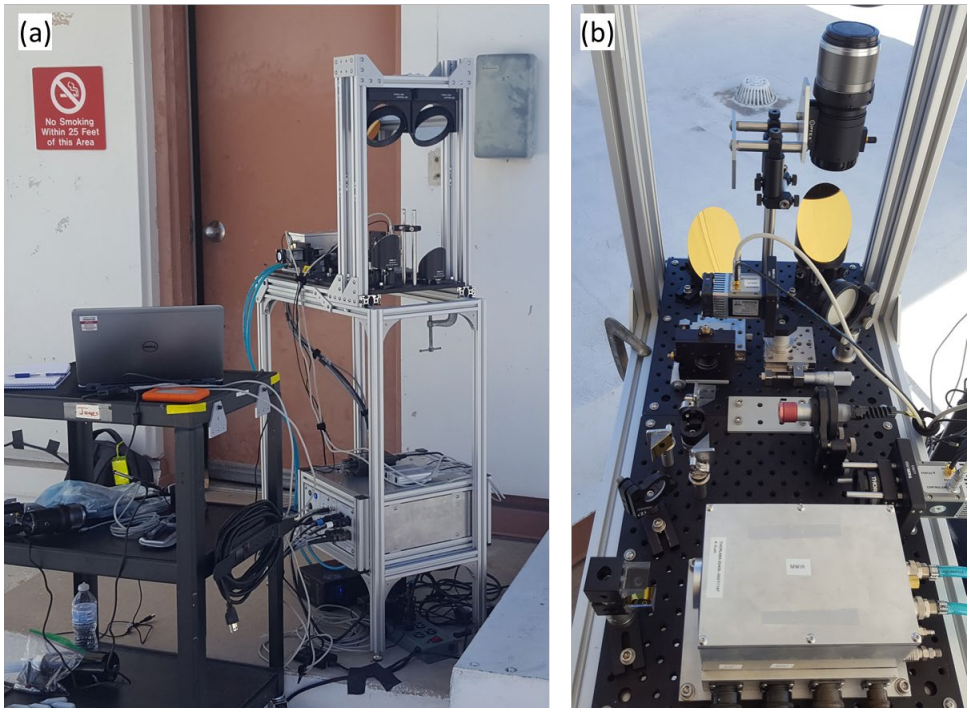

Figure 32: Photographs of previous system, before upgrades.

To remedy these previous issues, several upgrades were made as part of the preparation for the EMRTC experiments. Figure 33 shows photographs of the system after the upgrades were performed. The stand assembly was improved to have a larger footprint and better gusseting, both of which improved stability. The attachment of the optical platform to the stand was also improved to be more rigid. The optical platform was completely enclosed by aluminum framing, protecting the assembly when placed into the shipping case. The mast assembly holding the steering mirrors was shortened so that the mast assembly could be easily removed for shipping and re-attached quickly on-site. The footprint of the optical platform (300x600 mm) was not changed as it was based on a standard optical breadboard; however, the overall height of the system was reduced.

The most significant changes to the optical configuration were the mounting and alignment of the visible alignment camera. Previously, the camera was inserted and removed from the beam

path between the OAP and the Steering Mirrors. The camera had to be removed from the system for shipping which led to additional re-alignment time after repacking. To reduce the setup time, the camera was moved to be fixed in position within the optical platform. Instead of removing/replacing the entire camera as was previously done, now the beam path was switched by inserting/removing flat mirrors on indexed magnetic mounts placed between the OAPs and steering mirrors. This approach was found to decrease setup and alignment time; however, it is still in need of improvement for future systems. In the future, we plan to fully integrate a visible CMOS array into the optical system using the OAP combined with a secondary mirror to perform the visible alignment. By doing this, the visible alignment image will be even better registered with the infrared ECQCL beam because the OAP will be used for both systems.

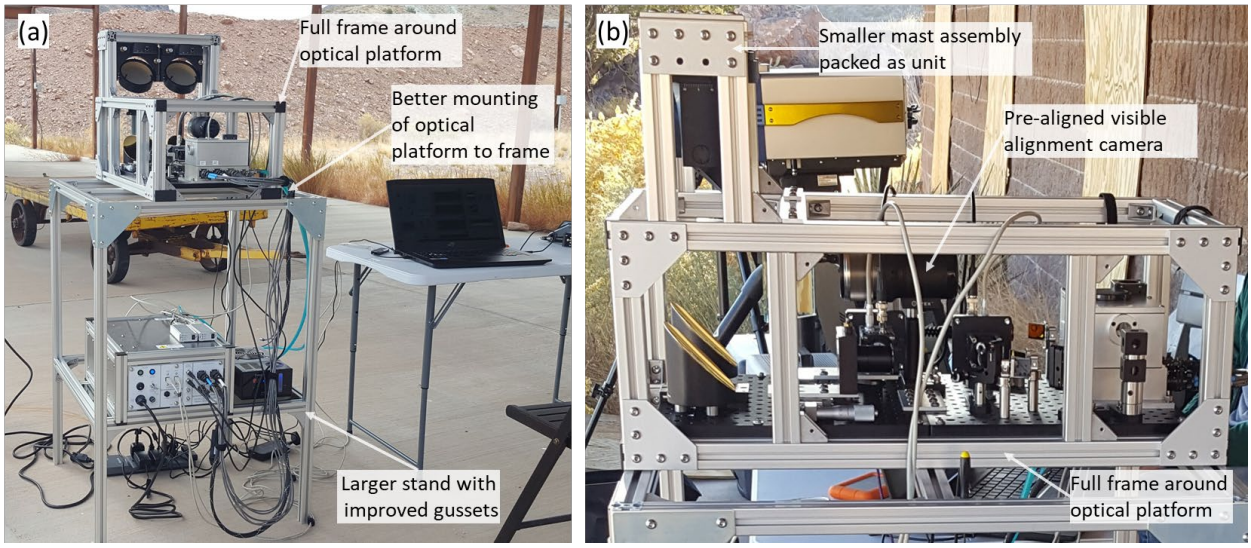

Figure 33: Photographs of system after upgrades.

Appendix C – Measurement Results From 11/07/2019

The measurements from 11/07 were performed with the ECQCL system at a different location and the results are not directly relevant for the main plume release studies. However, the system was operated most of the day and local releases of F152a were performed. Figure 34 shows measurement results from 11/07. The times of local F152a releases are noted. The small increased signals in SF_6 and N_2O are not real detections, but instead result from crosstalk during large absorption from F152a. When the F152a absorption becomes too large, the total power on the detector becomes small and noise increases. The decrease in power at the times of large F152a signals is also visible in Figure 34. Future work plans to modify the detection algorithm to account automatically for the reduction in power when large absorption signals are present, and thereby reduce the amount of crosstalk between detection channels.

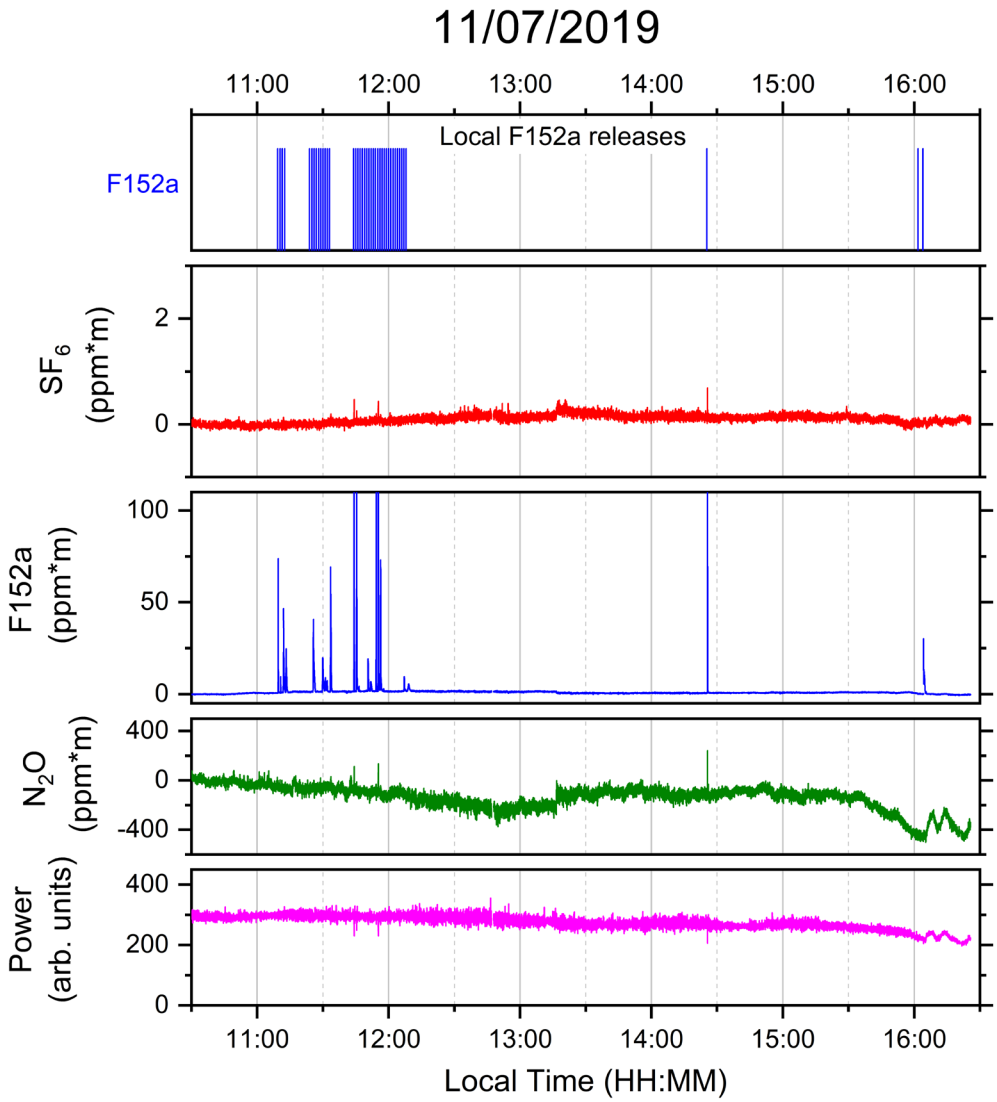

Figure 34: Measurement results from 11/07.

Figure 35 shows details for the series of local F152a releases.

Error! Reference source not found. provides a list of the times and locations for the releases. The release series in total consumed an entire can of F152a air duster, which has a net weight of 283 g. The releases were each timed to be of 5 s duration. Assuming the mass released was proportional to the release duration, and constant from start to finish, each release contained 7.3 g of F152a. It was likely that the later releases probably contained slightly less F152a due to the pressure reduction in the container from start to finish.

The releases were not all detected, and those that were detected showed different magnitudes and time dependence, due to variations in release point relative to the measurement path and wind direction.

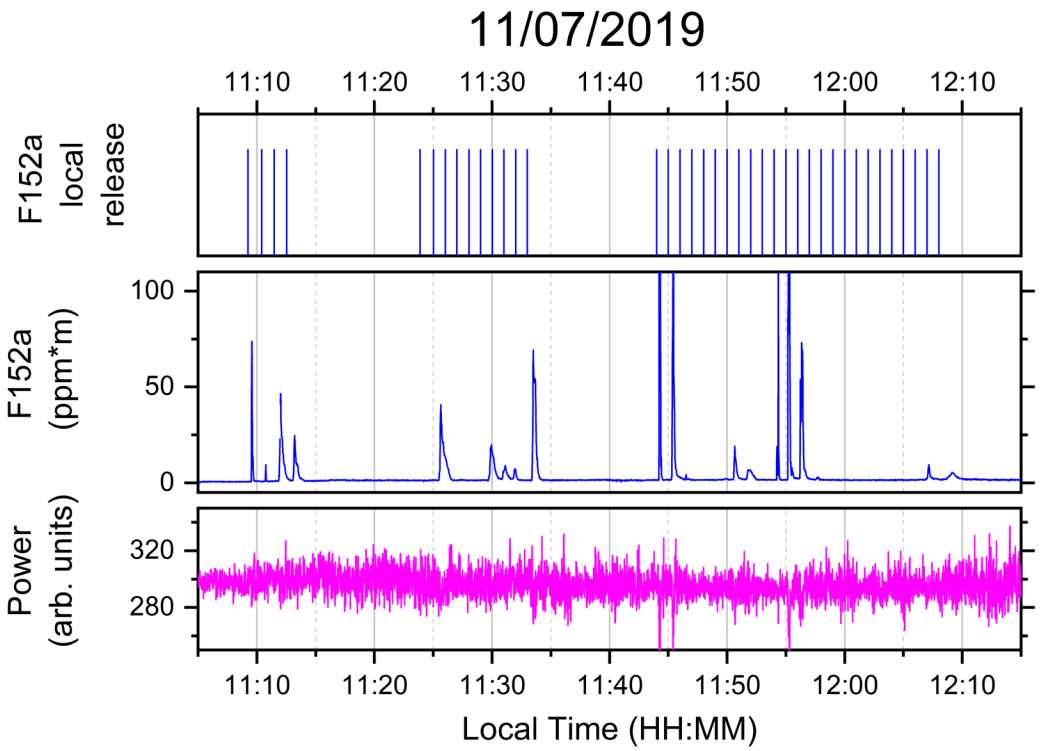

Figure 35: Measurement results for series of local F152a releases on 11/07.

Table 8: Times and locations of local F152a releases on 11/07

Local time	Latitude (N)	Longitude (W)		Local time	Latitude (N)	Longitude (W)
	34 degrees	106 degrees			34 degrees	106 degrees
(hh:mm:ss)	(minutes)	(minutes)		**(hh:mm:ss)**	(minutes)	(minutes)
11:09:15	3.291	56.426		**11:51:00**	3.322	56.423
11:10:25	3.307	56.422		**11:52:00**	3.322	56.423
11:11:28	3.328	56.418		**11:53:00**	3.322	56.423
11:12:32	3.344	56.412		**11:54:00**	3.291	56.430
11:23:53	3.336	56.433		**11:55:00**	3.271	56.439
11:25:01	3.333	56.423		**11:56:00**	3.261	56.441
11:26:01	3.332	56.411		**11:57:00**	3.257	56.433
11:27:00	3.329	56.401		**11:58:00**	3.261	56.432
11:28:02	3.348	56.413		**11:59:00**	3.273	56.428
11:29:01	3.355	56.428		**12:00:00**	3.286	56.426
11:30:01	3.364	56.429		**12:01:00**	3.300	56.421
11:31:01	3.358	56.415		**12:02:00**	3.316	56.417
11:32:01	3.333	56.425		**12:03:00**	3.335	56.412
11:33:00	3.307	56.427		**12:04:00**	3.346	56.408
11:44:00	3.280	56.432		**12:05:00**	3.347	56.418
11:45:00	3.298	56.428		**12:06:00**	3.352	56.433
11:46:00	3.323	56.423		**12:07:00**	3.355	56.447
11:47:00	3.351	56.416		**12:08:00**	3.331	56.434
11:48:00	3.360	56.411				
11:49:00	3.347	56.414				
11:50:00	3.330	56.422				

Figure 36 shows a zoom of the first 4 local F152a releases. Note that the data has been plotted at 10 Hz for this and the following figures, to better show the fast dynamics of the closer range F152a measurements. A time delay between release and detection is apparent due to the plume propagation time. In addition, the detection time is longer than 5 s due to the wind direction being nearly co-aligned with the measurement path. Also visible near 11:12 is a period when the return power dropped to nearly zero. This resulted periodically throughout the day as vehicles passed through the measurement path (which traversed a roadway). The measurement results have been filtered to remove points at which the return power was close to zero.

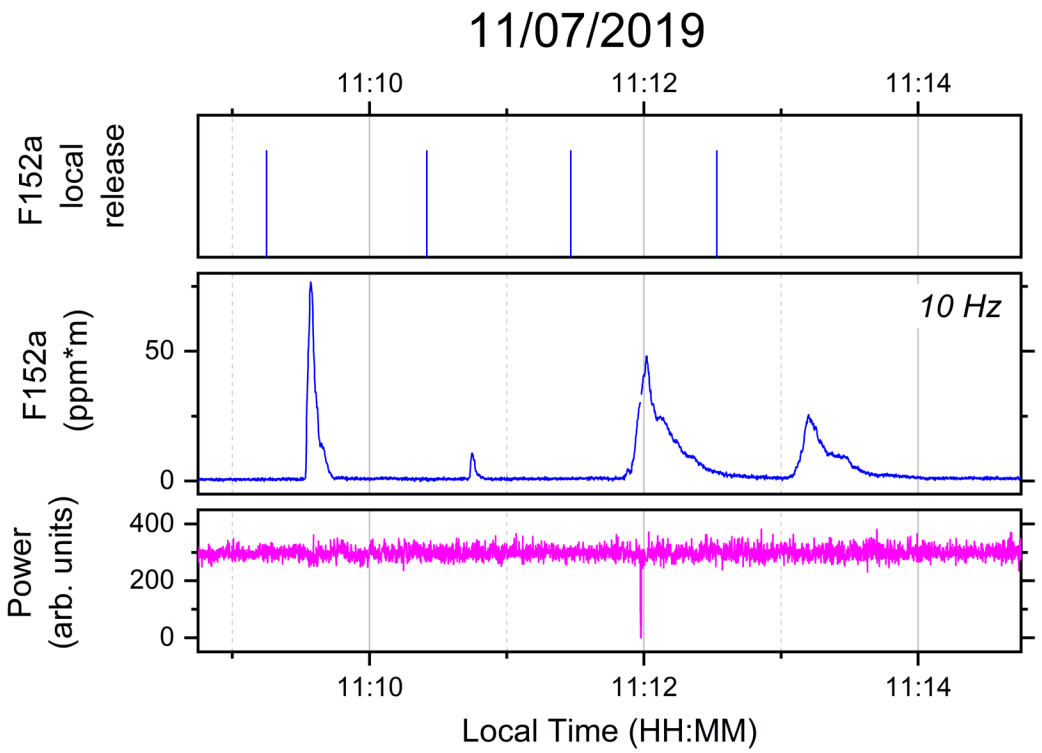

Figure 36: Measurement results for set of 4 local F152a releases.

Figure 37 shows measurement results for the second set of F152a releases. Figure 38 shows results for the third set of F152a releases, this time with the F152a column density plotted on a logarithmic scale due to the large dynamic range of column densities detected.

A more detailed analysis of the measurement results from 11/07 may be performed in the future if wind data is available.

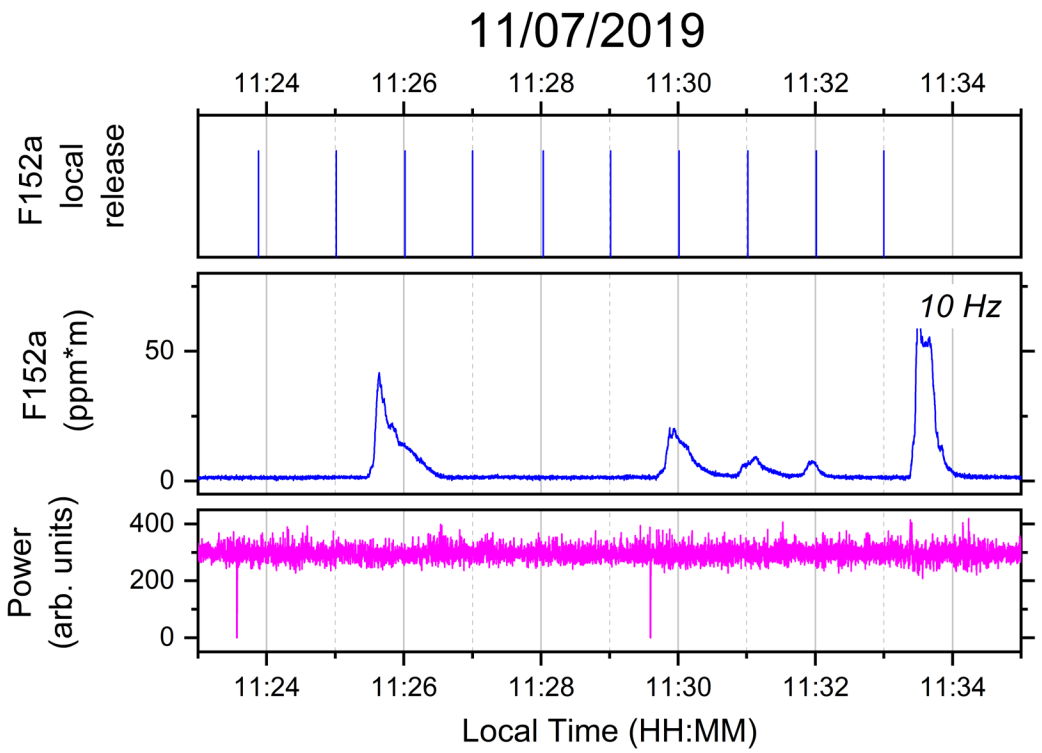

Figure 37: Measurement results for second set of local F152a releases.

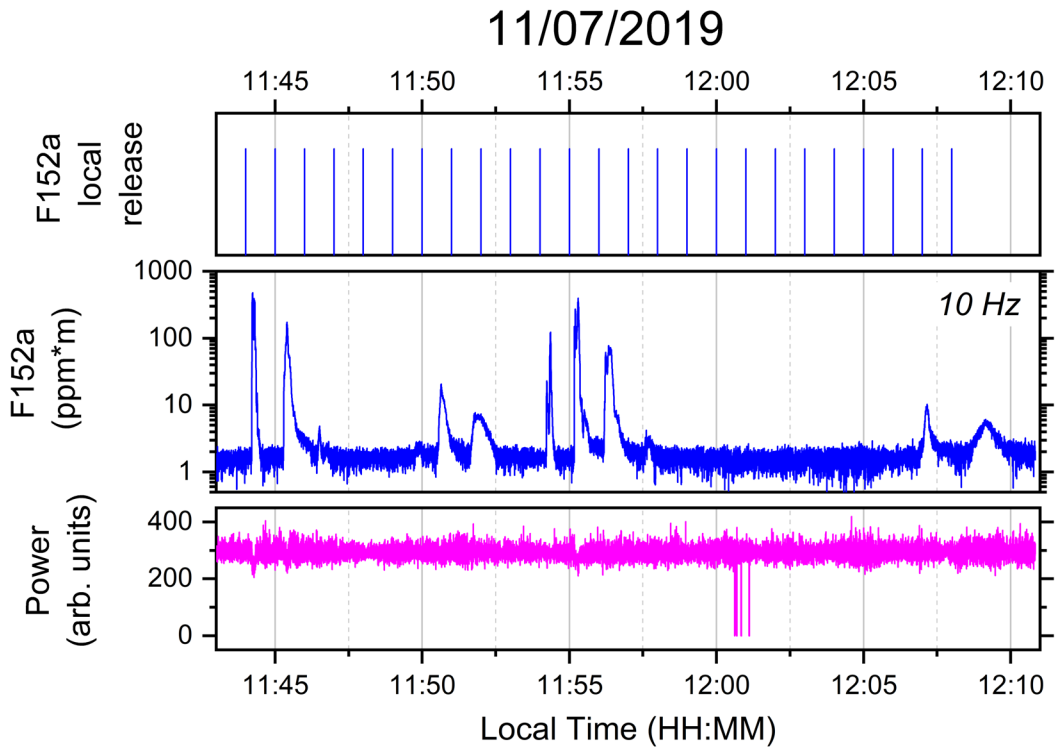

Figure 38: Measurement results for third set of local F152a releases.

Appendix D – Data Summary Tables

The following sections list the raw binary data files acquired using the swept-ECQCL system along with measurement notes taken on-site.

11/04/2019

Filename	Size (GB)	Scans	Start time	End time	Notes taken onsite
EMRTC_retro_1stlt_110419_135113	3.6	249120	14:51:25	15:01:48	After initial alignment of system
EMRTC_retro_2rel_110419_140148	5.8	398440	15:01:51	15:18:28	plume release at ~15:11
EMRTC_retro_2rel_b_110419_141828	7.1	486480	15:18:31	15:38:48	more plume releases
EMRTC_retro_etalonzero_110419_143858	0.3	22720	15:39:19	15:40:15	etalon scans and detector zeros
EMRTC_retro_F152a_local_110419_144501	1.3	90040	15:45:02	15:48:47	small F152a releases at little eagle site
EMRTC_retro_bakckground_110419_144908	5.4	369400	15:49:12	16:04:35	background - need to verify no releases
EMRTC_retro_top_release_110419_150435	9.1	622000	16:04:35	16:30:30	plume release at 16:10
EMRTC_retro_top_release_etalonzero_110419_153044	0.3	22760	16:30:46	16:31:43	etalon scans and detector zeros
EMRTC_retro_top_release_F152a_110419_153150	0.1	8440	16:31:51	16:32:12	small F152a releases at little eagle site

11/05/2019

Filename	Size (GB)	Scans	Start time	End time	Notes
EMRTC_etalonzero_110519_085916	0.3	20240	9:59:23	10:00:13	etalon scans and detector zeros
EMRTC_F152a_110519_090024	0.2	12040	10:00:45	10:01:15	small F152a releases at little eagle site
EMRTC_background_110519_090124	2.2	152800	10:01:28	10:07:50	background - need to verify no releases
EMRTC_background_110519_101324	3	206840	10:13:36	10:22:13	background - need to verify no releases
EMRTC_background_110519_102213	0.5	35920	10:22:13	10:23:43	background - need to verify no releases
EMRTC_background_110519_102343	0.6	39840	10:23:43	10:25:23	background - need to verify no releases
EMRTC_etalonzero_110519_102656	0.2	16800	10:26:57	10:27:39	etalon scans and detector zeros
EMRTC_plume_110519_102804	4.7	323960	10:28:07	10:41:36	mostly background - may be plumes near end
EMRTC_plume_110519_104136	4.8	328560	10:41:36	10:55:18	plume releases
EMRTC_plume_110519_105517	1.4	98600	10:55:18	10:59:24	plume releases
EMRTC_F152a_local_110519_110511	0.6	39640	11:05:26	11:07:05	small F152a releases at little eagle site
EMRTC_background_110519_110715	5.3	361800	11:07:53	11:22:58	background - need to verify no releases

EMRTC_background_110519_112257	7.5	510320	11:22:58	11:44:14	background - need to verify no releases
EMRTC_background_110519_114413	4.4	297480	11:44:14	11:56:37	background - need to verify no releases
EMRTC_plume_110519_115637	2.9	200080	11:56:37	12:04:57	SF6 and N2O plume release at 12:05
EMRTC_plume_110519_120457	5	338680	12:04:58	12:19:04	
EMRTC_plume_110519_121904	4.1	285480	12:19:04	12:30:58	
EMRTC_plume_110519_123057	7	478360	12:30:58	12:50:54	F152a and SF6 plume release at 12:35
EMRTC_plume_110519_125053	8	549240	12:50:54	13:13:47	
EMRTC_plume_110519_131347	10.3	706320	13:13:47	13:43:13	realigned system after this file
EMRTC_plume_110519_134441	7.2	490840	13:44:42	14:05:09	F152a and SF6 plume release at 1:45
EMRTC_plume_110519_140509	5.3	359080	14:05:09	14:20:07	F152a and SF6 plume release at 2:05
EMRTC_plume_110519_142007	1.5	104000	14:20:07	14:24:27	
EMRTC_etalonzero_110519_142427	0.4	24560	14:24:27	14:25:28	etalon scans and detector zeros
EMRTC_F152alocal_110519_142537	0.1	8000	14:25:40	14:26:00	small F152a releases at little eagle site
EMRTC_plume_110519_142607	8	547440	14:26:08	14:48:57	F152a and SF6 plume release at 2:31
EMRTC_plume_110519_144856	5.8	394720	14:48:57	15:05:24	
EMRTC_plume_110519_150523	2.2	148680	15:05:24	15:11:35	
EMRTC_plume_110519_151135	5.7	389520	15:11:35	15:27:49	SF6 plume release at 3:12
EMRTC_fixed_110519_152856	*0.7*	48640	15:28:59	15:31:00	*fixed wavelength data*
EMRTC_detzero_110519_153109	*0.03*	2480	15:31:18	15:31:24	*detector zero for fixed wavelength*
EMRTC_reducedrange01_110519_153501	*0.7*	50400	15:35:04	15:37:10	*reduced scan range to acquire higher resolution H2O data*
EMRTC_etalonzero_110519_153710	*0.3*	22560	15:37:10	15:38:07	*etalon scans and detector zeros*
EMRTC_reducedrange01_110519_153820	*4.4*	302360	15:38:24	15:51:00	*F152a local release at 3:43. Smoke plume at 3:45-3:50*
EMRTC_plume_110519_155110	8.3	567560	15:51:12	16:14:51	Full range. SF6 release at 3:55

11/06/2019

Filename	Size (GB)	Scans	Start time	End time	Notes
EMRTC_etalonzero_110619_094928	0.2	16360	9:49:30	9:50:11	etalon scans and detector zeros
EMRTC_F152a_110619_095019	0.2	12640	9:50:26	9:50:57	small F152a releases at little eagle site
EMRTC_background_110619_095104	1.8	124000	9:51:20	9:56:30	background
EMRTC_plume_110619_095629	9.3	632480	9:56:30	10:22:51	SF6 release at 10:07

EMRTC_plume_110619_102250	8	543280	10:22:51	10:45:29	light rain
EMRTC_plume_110619_104529	4.9	335920	10:45:29	10:59:29	
EMRTC_plume_110619_111444	5	343920	11:14:45	11:29:05	
EMRTC_plume_110619_112905	4.2	287640	11:29:05	11:41:04	
EMRTC_plume_110619_114104	6.9	471760	11:41:04	12:00:43	SF6 release at 11:45
EMRTC_plume_110619_120043	6.7	458480	12:00:44	12:19:50	
EMRTC_plume_110619_121949	5.1	350680	12:19:50	12:34:26	SF6 release at 12:20. light rain
EMRTC_plume_110619_123426	3	203920	12:34:27	12:42:56	
EMRTC_plume_110619_124256	7.4	508040	12:42:56	13:04:06	SF6 release at 12:45
EMRTC_etalonzero_110619_130414	0.2	15080	13:04:16	13:04:53	etalon scans and detector zeros
EMRTC_F152a_110619_130459	0.3	19280	13:05:02	13:05:50	small F152a releases at little eagle site. Realigned after this data
EMRTC_plume_110619_130930	4.2	287080	13:09:37	13:21:35	light rain. signal level decreasing, likely due to humidity increase

11/07/2019

Filename	Size (GB)	Scans	Start time	End time	Notes
EMRTC_etalonzero_110719_102528	0.3	19080	10:25:30	10:26:18	etalon scans and detector zeros
EMRTC_F152a_110719_102625	0.5	32880	10:26:45	10:28:07	small local F152a releases near system
EMRTC_background_110719_102835	8	548840	10:28:38	10:51:31	background
EMRTC_background_110719_105130	5.3	361640	10:51:31	11:06:35	background
EMRTC_F152plumetests_110719_110634	22.6	1542200	11:06:35	12:10:50	F152 controlled release series (see notes)
EMRTC_background_110719_121050	0.3	23480	12:10:50	12:11:49	background
EMRTC_background_110719_121149	11.7	799680	12:11:49	12:45:08	background
EMRTC_background_110719_124508	0.6	44200	12:45:08	12:46:59	background
EMRTC_etalonzero_110719_124703	0.3	17120	12:47:05	12:47:48	etalon scans and detector zeros
EMRTC_background_110719_124756	8.3	564640	12:47:59	13:11:31	background
EMRTC_background_110719_131131	12.4	848080	13:11:31	13:46:51	background
EMRTC_background_110719_134651	12.7	867840	13:46:51	14:23:01	background
EMRTC_background_110719_142300	0.8	57360	14:23:01	14:25:24	background
EMRTC_F152tests_110719_142524	0.7	46800	14:25:24	14:27:21	small local F152a releases near system

EMRTC_background_110719_142721	5	340800	14:27:21	14:41:33	background
EMRTC_background_110719_144133	11.7	795440	14:41:33	15:14:42	background
EMRTC_background_110719_151442	4.8	326720	15:14:42	15:28:19	background
EMRTC_drive_110719_152818	18.5	1261640	15:28:19	16:20:53	drove to valley center site and back. Released F152a at 4:02 in canyon. Released F152a from truck at 4:04 near beam path
EMRTC_etalonzero_110719_162053	0.2	14960	16:20:53	16:21:30	etalon scans and detector zeros
EMRTC_background_110719_162130	1.5	99680	16:21:30	16:25:40	background

References

1. M. C. Phillips, B. E. Bernacki, S. S. Harilal, J. Yeak, and R. J. Jones, "Standoff chemical plume detection in turbulent atmospheric conditions with a swept-wavelength external cavity quantum cascade laser," Optics Express **28**, 7408-7424 (2020).
2. I. E. Gordon, L. S. Rothman, C. Hill, R. V. Kochanov, Y. Tan, P. F. Bernath, M. Birk, V. Boudon, A. Campargue, K. V. Chance, B. J. Drouin, J. M. Flaud, R. R. Gamache, J. T. Hodges, D. Jacquemart, V. I. Perevalov, A. Perrin, K. P. Shine, M. A. H. Smith, J. Tennyson, G. C. Toon, H. Tran, V. G. Tyuterev, A. Barbe, A. G. Csaszar, V. M. Devi, T. Furtenbacher, J. J. Harrison, J. M. Hartmann, A. Jolly, T. J. Johnson, T. Karman, I. Kleiner, A. A. Kyuberis, J. Loos, O. M. Lyulin, S. T. Massie, S. N. Mikhailenko, N. Moazzen-Ahmadi, H. S. P. Muller, O. V. Naumenko, A. V. Nikitin, O. L. Polyansky, M. Rey, M. Rotger, S. W. Sharpe, K. Sung, E. Starikova, S. A. Tashkun, J. Vander Auwera, G. Wagner, J. Wilzewski, P. Wcislo, S. Yu, and E. J. Zak, "The HITRAN2016 molecular spectroscopic database," Journal of Quantitative Spectroscopy & Radiative Transfer **203**, 3-69 (2017).
3. S. W. Sharpe, T. J. Johnson, R. L. Sams, P. M. Chu, G. C. Rhoderick, and P. A. Johnson, "Gas-phase databases for quantitative infrared spectroscopy," Applied Spectroscopy **58**, 1452-1461 (2004).
4. M. C. Phillips, M. S. Taubman, B. E. Bernacki, B. D. Cannon, R. D. Stahl, J. T. Schiffern, and T. L. Myers, "Real-time trace gas sensing of fluorocarbons using a swept-wavelength external cavity quantum cascade laser," Analyst **139**, 2047-2056 (2014).

Pacific Northwest National Laboratory

902 Battelle Boulevard
P.O. Box 999
Richland, WA 99354
1-888-375-PNNL (7665)

www.pnnl.gov